Earth and Planetary Science Letters 285 (2009) 227–242

Contents lists available at ScienceDirect

Earth and Planetary Science Letters

journal homepage: www.elsevier.com/locate/epsl

Volcanism on Mercury: Evidence from the first MESSENGER flyby for extrusive and explosive activity and the volcanic origin of plains

James W. Head [a,*], Scott L. Murchie [b], Louise M. Prockter [b], Sean C. Solomon [c], Clark R. Chapman [d], Robert G. Strom [e], Thomas R. Watters [f], David T. Blewett [b], Jeffrey J. Gillis-Davis [g], Caleb I. Fassett [a], James L. Dickson [a], Gareth A. Morgan [a], Laura Kerber [a]

[a] Department of Geological Sciences, Brown University, Providence, RI 02912, USA
[b] Johns Hopkins University Applied Physics Laboratory, Laurel, MD 20723, USA
[c] Department of Terrestrial Magnetism, Carnegie Institution of Washington, Washington, DC 20015, USA
[d] Southwest Research Institute, Boulder, CO 80302, USA
[e] Lunar and Planetary Laboratory, University of Arizona, Tucson, AZ 85721, USA
[f] Center for Earth and Planetary Studies, National Air and Space Museum, Smithsonian Institution, Washington, DC 20560, USA
[g] Hawaii Institute of Geophysics and Planetology, University of Hawaii, Honolulu, HI 96822, USA

ARTICLE INFO

Article history:
Accepted 4 March 2009
Available online 28 April 2009

Editor: T. Spohn

Keywords:
Mercury
volcanism
plains
Caloris basin
MESSENGER

ABSTRACT

The first MESSENGER flyby of Mercury obtained images of 21% of the surface not seen by Mariner 10, including the center and western half of the Caloris basin and regions near the terminator that show details of the nature of smooth and intercrater plains. These new data have helped to address and resolve a series of longstanding questions on the existence and nature of volcanism on Mercury and the distribution of volcanic materials. Data from the Mercury Dual Imaging System (MDIS) on the MESSENGER spacecraft have shown the following: (1) Numerous volcanic vents, in the form of irregularly shaped rimless depressions, are concentrated around the interior edge of the Caloris basin. (2) These vents appear to be sources for effusive volcanism that in one case built a shield in excess of 100 km in diameter and in some cases formed bright haloes around the vents that are interpreted to represent pyroclastic eruptions. (3) Lobate margins of plains units, seen previously in Mariner 10 data, are documented in MESSENGER images with more clarity and are often distinctive in morphology and color properties, supporting the interpretation that these features are the edges of lava flow units. (4) The interior of the Caloris basin is filled with plains units spectrally distinctive from the rim deposits, and comparison with the lunar Imbrium basin and superposed impact crater stratigraphy provide evidence that these units are volcanic in origin; detailed differences in the mineralogy of lava flow units, so prominent in Imbrium, are not seen in the Caloris interior. (5) Some of the smooth plains surrounding the exterior of the Caloris basin show distinct differences in color and morphological properties, supporting a volcanic origin. (6) Some smooth and intercrater plains units distant from the Caloris basin show evidence of flooding and embayment relations unrelated to Caloris ejecta emplacement; local and regional geological and color relationships support a volcanic origin for these plains. (7) Large impact craters show a sequence of embayment of interior floor and exterior ejecta deposits that supports a volcanic origin for the embayment and filling processes. (8) Crater embayment and flooding relationships in selected areas suggest volcanic plains thicknesses of many hundreds of meters and local thicknesses inside impact craters of up to several kilometers. (9) Impact crater size–frequency distributions for Caloris exterior deposits, including the facies of the Caloris Group and relatively high- and low-albedo smooth plains, show that they are younger than plains interior to Caloris and thus must be dominantly the product of post-Caloris volcanism. These new data provide evidence that supports and confirms earlier hypotheses from Mariner 10 data that volcanism was important in shaping the surface of Mercury. The emerging picture of the volcanic style of Mercury is similar to that of the Moon, the other small, one-plate planetary body: there are no major shield volcanoes (e.g., comparable to Tharsis Montes on Mars), shallow magma reservoirs are rare, and there is little evidence for surface deformation or long-lived volcanic sources related to sites of upwelling mantle. The close association of volcanic plains and surface deformation features suggests that future observations and analyses can help document the relation between the volcanic flux and the evolving state and magnitude of stress in the lithosphere of Mercury.

* Corresponding author.
E-mail address: James_Head_III@Brown.edu (J.W. Head).

0012-821X/$ – see front matter © 2009 Elsevier B.V. All rights reserved.
doi:10.1016/j.epsl.2009.03.007

1. Introduction and background

One of the major goals of the MErcury Surface, Space ENvironment, GEochemistry, and Ranging (MESSENGER) mission is to investigate the history of volcanism on Mercury (Solomon et al., 2007; Head et al., 2007). For terrestrial planetary bodies, volcanism–the eruption of internally derived magma and formation of surface deposits–provides important clues to interior melt generation in space and time and to the general thermal evolution of the planet.

On the Moon there are distinctive composition-related albedo variations between the volcanic mare lowlands and the cratered highlands. Within the lunar highlands, smooth plains units with a higher albedo than the maria (Cayley Formation) were also mapped and interpreted to be volcanic (Wilhelms and McCauley, 1971). However, upon landing on the Cayley plains, it became apparent to Apollo 16 Astronauts Young and Duke that the Cayley Formation consisted of impact breccias (Young et al., 1972), suggesting that the intermediate-albedo lunar upland plains resulted from emplacement of impact ejecta rather than lavas (Oberbeck et al., 1974; Oberbeck, 1975; Wilhelms, 1976).

Mariner 10 arrived at Mercury shortly after Apollo 16, and image data revealed the presence of two smooth plains units (Fig. 1) that appeared similar in smoothness and embayment relations to the lunar maria. These widespread plains deposits, occurring as relatively smooth surfaces between craters (intercrater plains), and as apparently ponded material (smooth plains and Caloris floor plains), were proposed by most investigators to be volcanic in origin (Murray et al., 1975; Trask and Guest, 1975; Strom et al., 1975; Strom, 1977; Dzurisin, 1978). Others, however, argued that the plains on Mercury might represent basin ejecta (Wilhelms, 1976), deposits similar to those found at the Apollo 16 landing site on the Moon (e.g., Oberbeck et al., 1977). One of the problems in confidently determining a volcanic or

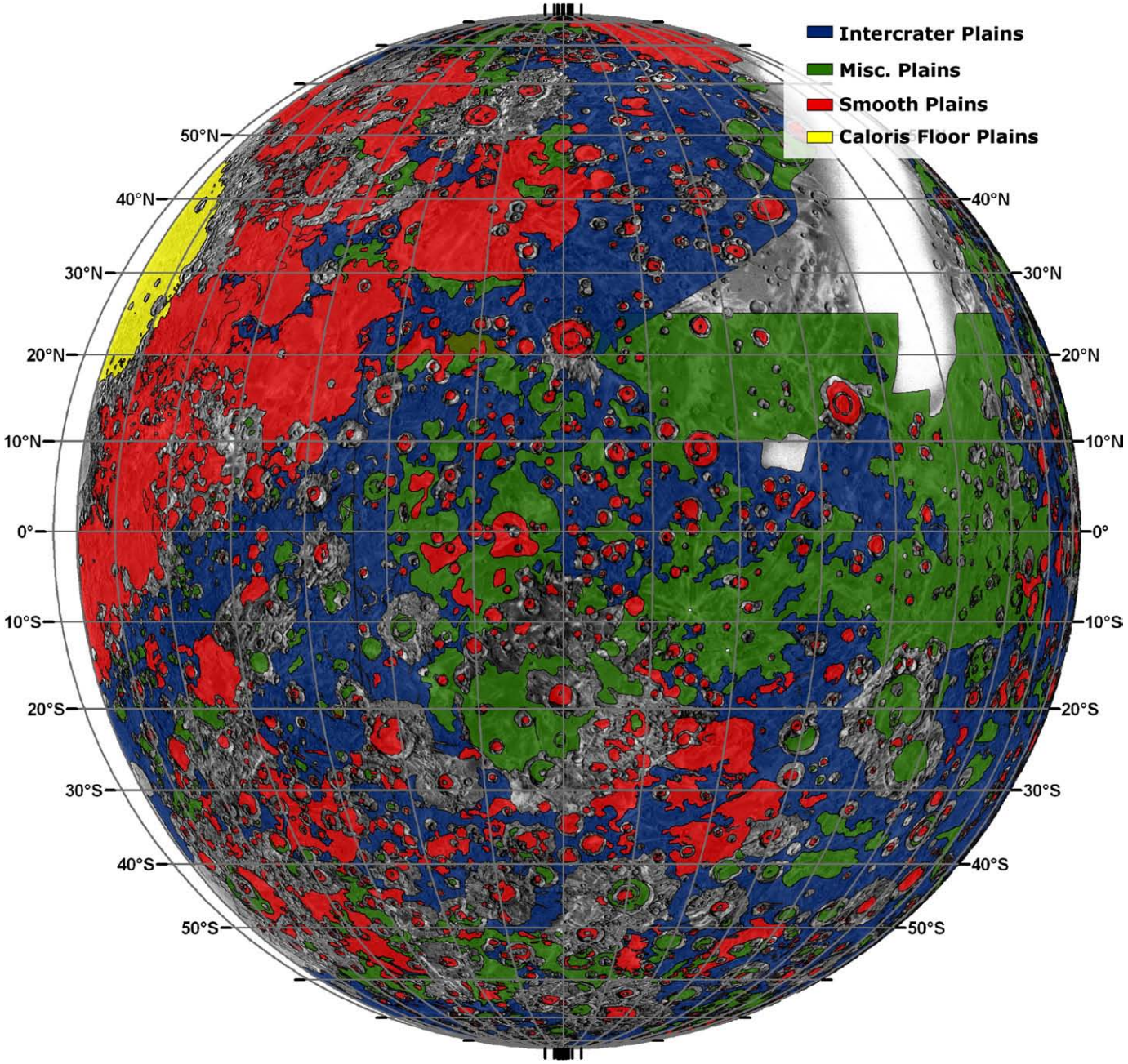

Fig. 1. Distribution of plains units from Mariner 10. The map is compiled from integrating the geological maps derived from Mariner 10 images (Schaber and McCauley, 1980; De Hon et al., 1981; Guest and Greeley, 1983; McGill and King, 1983; Spudis and Prosser, 1984; Trask and Dzurisin, 1984; King and Scott, 1990; Strom et al., 1990).

impact origin for the plains on Mercury is the relatively low resolution and variable viewing geometry of the Mariner 10 images, often insufficient to resolve lunar-like volcanic features such as flow fronts, vents, and small domes (Schultz, 1977; Malin, 1978; Milkovich et al., 2002).

Nonetheless, crater counts of Caloris basin ejecta facies and smooth plains deposits indicated that the smooth plains were emplaced after the Caloris basin formed (Spudis and Guest, 1988), and on this basis they were interpreted to be the product of volcanic eruptions, not contemporaneous ejecta emplacement. Furthermore, reprocessed Mariner 10 color data provided additional evidence for the volcanic origin of the smooth plains (plains units with different color could be recognized and showed embayment relationships) and related candidate pyroclastic activity (distinctive color units draped over

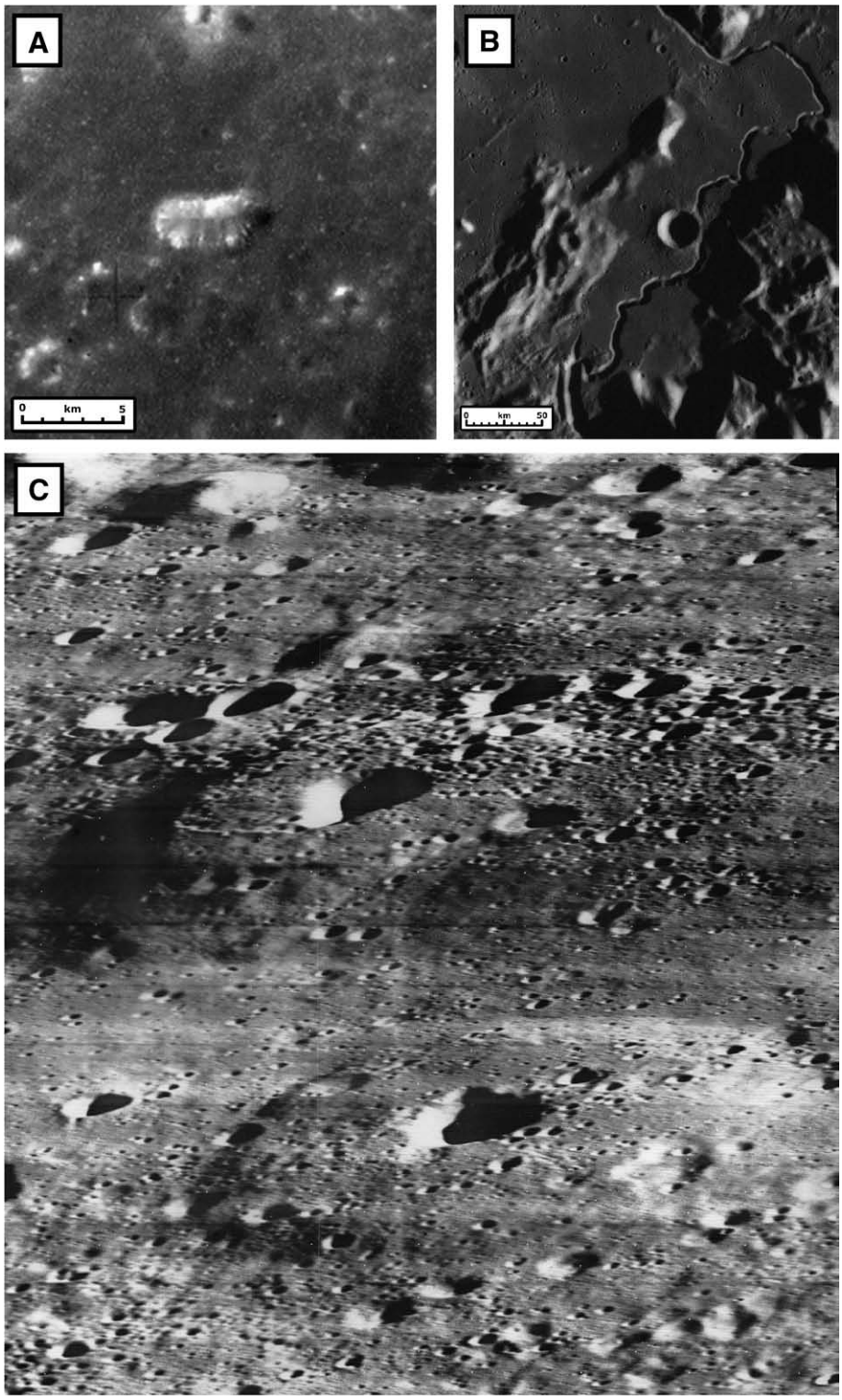

Fig. 2. Lunar volcanic vents. (A) Rimless depression in the Sulpicius Gallus Formation, southwestern Serenitatis; depression is 5.6 km by 2.3 km. (Apollo Metric 1812). (B) Elongate depression and sinuous rille (Hadley Rille; Lunar Orbiter IV-102-H3). (C) Small shields near Hortensius crater (6.5°N, 28.0°W) (perspective view of rimless depressions on lunar mare domes; Lunar Orbiter III 123H2).

adjacent topography) (Robinson and Lucey, 1997). Exploring this conundrum, Head and Wilson (2001) assessed whether partial melting of the mantle could have occurred but extrusive volcanism be inhibited. They found that during ascent and eruption of magma under a range of conditions appropriate to Mercury, a thick, low-density crust could, as with the Moon (e.g., Head and Wilson, 1992), inhibit and potentially preclude dikes from rising to the surface and forming effusive eruptions. Invoking a global compressional state of stress in the lithosphere (e.g., Strom et al., 1975), Head and Wilson (2001) developed a scenario by which rising magma intruded the crust but did not reach the surface. Under such conditions the level of resurfacing or the array of volcanic landforms seen on the Moon, Mars, and Venus would not be expected.

That fundamental questions have persisted concerning the surface geology and thermal evolution of Mercury underscores the importance of the MESSENGER mission. One of the major goals of the mission is to provide information on the origin of surface plains deposits from imaging, spectroscopy, and altimetry. The mission will also assess the composition and evolution of the mantle and core by mapping surface mineralogy, elemental chemistry, tectonic features, and gravity and magnetic fields (Solomon et al., 2007). The Mercury Dual Imaging System (MDIS) (Hawkins et al., 2007) on MESSENGER provided high-resolution imaging and color data during the first Mercury flyby on January 14, 2008, for about 21% of the surface not previously seen by spacecraft, including the entire Caloris basin and surrounding plains, as well as areas viewed by Mariner 10 (Solomon et al., 2007, 2008). Preliminary analysis of these data revealed evidence for volcanic vents and edifices (Head et al., 2008), stratigraphic relationships suggesting volcanic fill of the Caloris basin interior (Murchie et al., 2008), different crater ages for plains units (Strom et al., 2008; Fassett et al., 2009–this issue), and distinctive differences in color data between numerous plains and surrounding uplands (Robinson et al., 2008), all supporting a volcanic origin for many occurrences of smooth plains. Here we provide a more detailed analysis and synthesis of the MDIS data related to extrusive volcanism. In a separate analysis we examine evidence for intrusive activity (Head et al., 2009–this issue).

MDIS is an articulated system with a multispectral wide-angle camera (WAC) and monochromatic narrow-angle camera (NAC) (Hawkins et al., 2007). During the first flyby, MDIS obtained 1213 science images, including two NAC mosaics (covering the circum-Caloris region with a spatial resolution of 200–300 m/pixel) and an 11-band WAC mosaic (covering the hemisphere at ~2.4 km/pixel). In preparation for these analyses, MDIS images were calibrated to

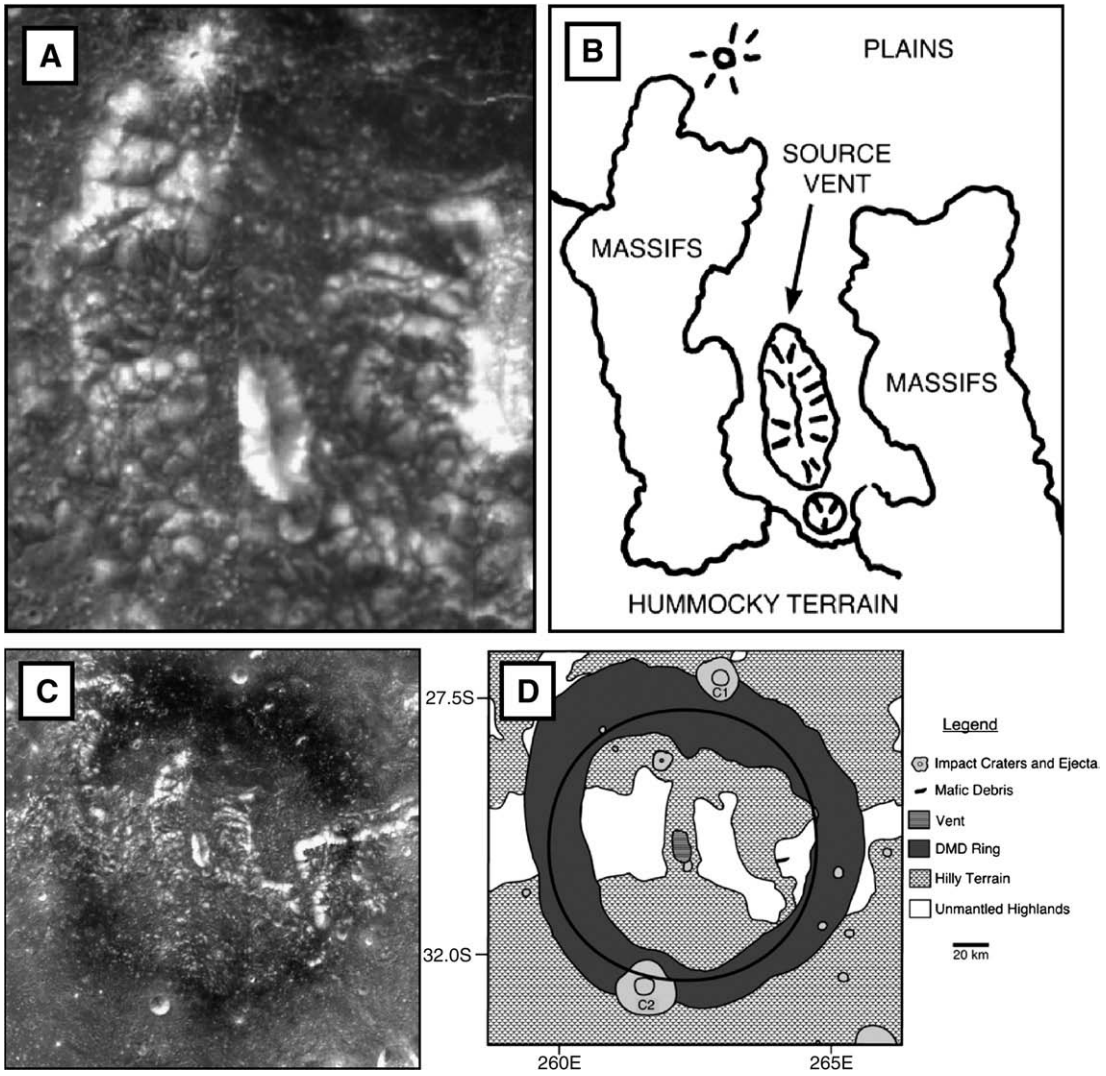

Fig. 3. Lunar elongated rimless depression and associated pyroclastic deposit in the southern part of the Orientale basin. (A) Elongated linear rimless depression at the center of a dark pyroclastic ring at the Outer Rook ring of the Orientale multi-ring basin. Linear depression, 7.5 × 16 km, interpreted to be the source vent for the dark pyroclastic ring. Clementine image (orbit 204). (B) Sketch map of (A). (C) Orientale dark pyroclastic ring deposit surrounding source vent (A). Clementine image (orbits 203–205). (D) Geologic sketch map of (C). (Modified from Head et al., 2002).

radiance factor and photometrically corrected to standard viewing geometry (Robinson et al., 2008). In a manner similar to other analyses (Robinson et al., 2008; Murchie et al., 2008; Blewett et al., 2009–this issue), principal component (PC) analysis of the WAC 11-band color data and spectral ratios was used to identify and map spectral contrasts between surface materials. The first principal component (PC1) emphasizes variations in reflectance, and the second (PC2) emphasizes spectral variations related to the physical state or chemistry of the material (predominantly slope of the spectral continuum). For related geological analyses, images were map-projected and coregistered using MDIS optical parameters, the Mercury and spacecraft ephemeris data, and knowledge of the orientation of both the spacecraft and the pivot of MDIS.

2. The circum-Caloris irregular rimless depressions: evidence for volcanic vents and shields

Volcanic vents and their surrounding deposits form the morphological and mineralogical features that permit the recognition of the process of volcanism on planetary bodies, the interpretation of specific volcanic styles, and the assessment of volumetric significance and duration of the process. On the Moon (Fig. 2), a wide range of volcanic vents are observed (Schultz, 1976b): (1) circular to elongate rimless depressions associated with pyroclastic deposits (Fig. 2A) (Lucchitta and Schmitt, 1974; Head and Wilson, 1979; Head et al., 2002; Gaddis et al., 2003); (2) summit pits on small, low shield volcanoes (Fig. 2C) (Head and Gifford, 1980); (3) circular and elongate depressions associated with sinuous rilles (Fig. 2B); (4) chains of craters thought to represent magmatic degassing; (5) circular to irregular craters associated with small cones; and (6) linear fissures from which lava flows emerge (Head, 1976).

Scalloped rimless depressions are very typical of volcanic source vents on the Earth, Moon, and other planets (Fig. 3) and are generally readily distinguished from impact craters, which also are depressions. Impact craters form from hypervelocity impacts that excavate material and deposit it as ejecta on and beyond the crater rim, with a systematic decrease in average thickness with radial range. Volcanic eruptions can also produce elevated landforms around vents, ranging from tephra cones around relatively small, short-lived eruptions to large shield-like structures around vents that are continuously active over longer time periods. Commonly these larger structures have very different exterior morphology and topography from impact craters, with sinuous flow lobes and shallow sloping flanks. Moreover, the structure of the craters themselves is also different. Impact craters show a distinctive and well-established transition in morphology with increasing size from simple circular bowl shapes to complex polygonal planforms and flat floors (e.g., Pike, 1988). Although scalloped rims commonly characterize the transition from simple to complex craters (the Mercury immature-complex crater class of Pike, 1988), all other impact crater characteristics are preserved and there is rarely confusion between these craters and those of volcanic origin, even in the case of degraded impact craters (which are always circular or elliptical, not irregular, and whose rims may decrease in elevation, but rarely disappear entirely).

Volcanic craters having diameters in excess of several hundred meters commonly form from magma migration in a shallow magma reservoir; growth of the magma reservoir causes inflation of the summit, and lateral intrusion and eruption causes deflation and collapse of the surface above the reservoir. For large edifices and reservoirs, successive stages of inflation and collapse of the reservoir lead to multiple intersecting depressions and to scalloping of the walls and rim of the depression as a whole (e.g., Crumpler et al., 1996; Wilson et al., 2001). These processes can lead to a variety of summit caldera sizes and shapes. For eruptions, edifice width and height are linked to the characteristics of the lavas and the duration of activity; high-effusion-rate, low-viscosity lavas can build broad low shields, while higher-viscosity lavas might build steeper and taller edifices. In summary, large scalloped depressions on top of edifices that are surrounded radially by lava flows (e.g., Olympus Mons) are clearly of volcanic origin. Intermediate-scale scalloped rimless depressions in the 10–20 km diameter range are unlikely to be primary impact craters but need to be examined on a case by case basis to distinguish them from highly degraded impact craters or very large secondary craters and crater clusters.

Such intermediate-scale rimless depressions on the Moon are often characterized by surrounding pyroclastic deposits. Along the southwestern margin of the Serenitatis basin (Fig. 2A), a dark mantling deposit, the Sulpicius Gallus Formation, is associated with a series of arcuate rilles and predates much of the later central mare fill (Carr, 1966). Linked to loading, flexure, and deformation associated with filling of the basin by mare deposits (Solomon and Head, 1979, 1980), these rilles and associated pyroclastic deposits are clearly

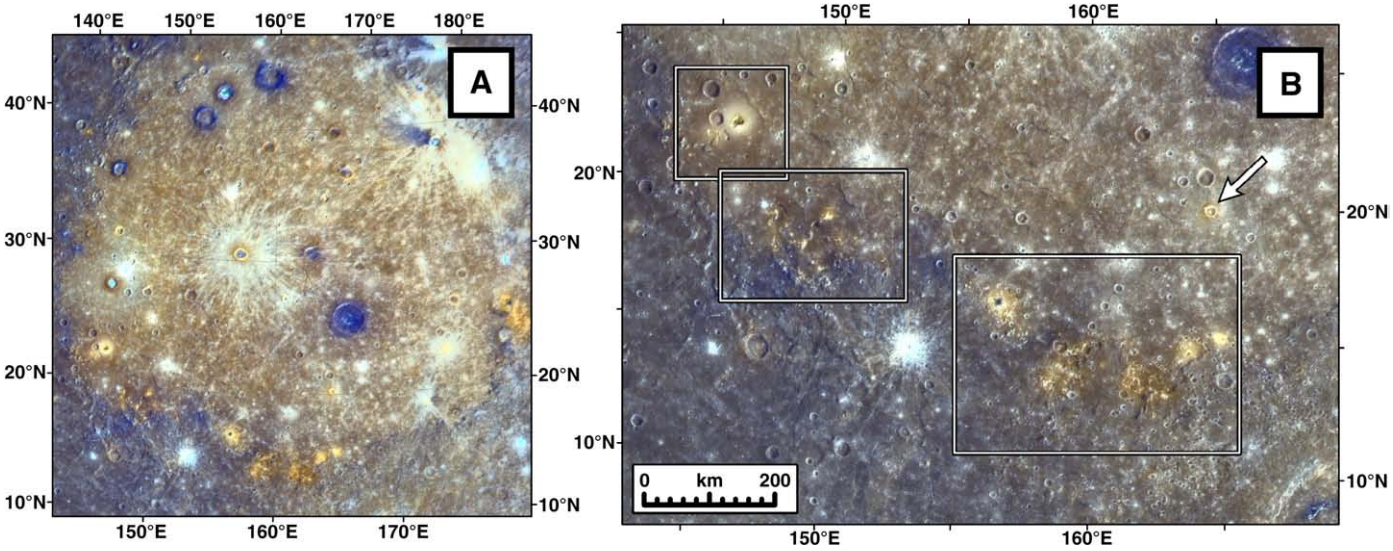

Fig. 4. Irregular rimless depressions inside the rim of the Caloris basin. (A) Color image of the Caloris basin interior showing the locations of the major color anomalies associated with the rimless depressions. Color images are RGB composites (red, inverse of PC2; green, PC1; blue, relative visible color, 430 nm/560 nm ratio; see Robinson et al., 2008 for details). (B) Southern part of the Caloris basin, showing the location of the major rimless depressions along the inner margin of the basin rim. Locations of Fig. 5A, B, and C are shown by boxes.

embayed by later central mare fill (Head, 1974a). A 5.5-km-long, kidney-shaped, rimless depression (Fig. 2A) is centrally located in the Sulpicius Gallus deposit, which is interpreted as a mantle of pyroclastic origin on the basis of geological and stratigraphic relationships (Head, 1974a), visual observations from orbit (Lucchitta and Schmitt, 1974), and spectral character (Gaddis et al., 2003). Exposures in the walls of the depression have been interpreted to represent ~50-m-thick deposits of pyroclastic material similar to those sampled in related deposits on the southeastern margin of Serenitatis basin at the Apollo 17 site (Lucchitta and Schmitt, 1974). A second example is seen associated with the Outer Rook ring of the Orientale basin (Fig. 3), where an elongate rimless depression 7.5 km by 16 km (Fig. 3A and B) centrally located within a ~150-km-diameter ring of dark mantle (Fig. 3C and D) is interpreted to be the source for the eruption that produced the spectrally distinct dark mantle ring (Head et al., 2002). As in the Serenitatis example, the close proximity of the rimless depression and pyroclastic deposit to the impact basin ring (Fig. 3C) suggests that the volcanism is associated with impact basin evolution.

Initial analysis of MESSENGER data from the first flyby revealed color and morphologic evidence for two types of volcanic vents around the Caloris basin inner margin (Robinson et al., 2008; Murchie et al., 2008; Head et al., 2008) (Fig. 4). Deposits surrounding one of these vents were interpreted to represent a shield-like structure more than 100 km in diameter (Head et al., 2008) (Fig. 5A). Other features are irregularly shaped rimless depressions with scalloped walls, similar to volcanic vents on the Moon (Figs. 2 and 3). These vent-like features on Mercury (Figs. 4B and 5A–C) are characterized by surrounding diffuse bright deposits (Head et al., 2008) that display distinctive color characteristics (a redder spectral continuum than other materials) different from fresh impact craters and also show no evidence of the ray-like patterns typical of impact craters (Murchie et al., 2008; Robinson et al., 2008). The diffuse bright deposits are interpreted to be of pyroclastic origin on the basis of their characteristics and proximity to the irregular depressions (Head et al., 2008; Murchie et al., 2008; Robinson et al., 2008; Kerber et al., 2009–this issue). Impact crater ejecta deposits surrounding craters of different sizes show evidence that material with similar spectral characteristics lies at relatively shallow depths below the central Caloris basin fill (Murchie et al., 2008) (Fig. 4A and B). Major outstanding questions are (1) What is the nature of the volcanism associated with these features and structures? (2) What is their spatial and temporal relation to the Caloris basin and its subsequent fill? (3) How are they related to the smooth plains that characterize the Caloris interior and exterior? (4) How are they related to the tectonic structures that characterize the Caloris basin interior? (5) Are similar features recognized in association with other impact craters and basins?

Geological analysis has revealed many additional aspects of these deposits that can help address these questions. The main occurrence of these features is along the southern margin of the Caloris basin interior (Figs. 4A–B and 5), where eight separate examples are found, and along the southeastern margin (Fig. 6), where a large deposit is seen that can now also be recognized in the Mariner 10 images. Two additional small deposits with similar color characteristics lie just inside the basin along its north–northwestern margin (Fig. 4A), but the morphological features are not very distinctive. The southeastern example is instructive because it can be observed in both MESSENGER and Mariner 10 image data, under two different illumination conditions (Fig. 6). The deposit was originally mapped as part of the extensive Caloris basin floor plains material, occurring in an alcove in the Caloris Montes Formation and the contiguous Odin Formation (Guest and Greeley, 1983) (Fig. 6A). A crater chain (cs4; red), about 135 km long, separates the main Caloris floor plains material from the alcove in which the rimless depressions occur, and two impact craters (c3 and c4, Fig. 6A) are superposed on the region. Although originally mapped as a c4 secondary crater chain (Guest and Greeley, 1983), the structure is long and continuous, unlike many crater chains that are more discontinuous, and appears to extend to the north and the south as a graben structure (the c3 crater is superposed on the southern transition). The color anomaly (Fig. 6C) is centered more on the two irregular depressions (two west-pointing arrows in Fig. 6A) than on the crater chain, but the proximity of the features is striking and very similar to the setting of the lunar southwestern Serenitatis graben/vent/pyroclastics relationship (Fig. 2A). The northern irregular depression is about 25 km in length and 12 km in width, and it has a distinctly scalloped flat rim with scallops in planform ranging from 4 to 10 km in width. The southern depression is about 10 km by 17 km and is more kidney-shaped in planform. Between the two depressions and the crater chain is a sinuous lobate scarp facing westward from the depression area and partly embaying the crater chain (small east-pointing arrow in Fig. 6A). Sinuous scarps elsewhere on Mercury have been interpreted as both tectonic features (wrinkle ridges) and candidate volcanic flow fronts (Strom et al., 1975). The extreme sinuosity of this scarp, its scarp-like rather than ridge-like nature (compare with wrinkle ridges west of the c4 crater), and its close proximity to the irregular depressions suggest that this may be a steep lava flow front (see also Wilson and Head, 2008). We interpret the two scalloped depressions discussed here (Fig. 6) to be of volcanic origin on the basis of: (1) their central location in the color anomaly, (2) their scalloped and rimless nature, (3) the associated lobate feature, and (4) their proximity to the elongated crater chain of apparent internal origin. Although available images are at the limits of resolution for detecting primary volcanic features such as sinuous rilles and volcanic cone fields (e.g., Milkovich et al., 2002), these findings suggest that the regions around the irregular depressions should be an important focus of the orbital phase of MESSENGER.

As outlined previously (Head et al., 2008), the largest and most prominent irregular rimless depression (Fig. 5A) is found atop a shield-like structure over 100 km in diameter, and the depression is surrounded by a prominent bright deposit with diffuse margins, interpreted to be of pyroclastic origin (Head et al., 2008; Murchie et al., 2008; Robinson et al., 2008; Kerber et al., 2009–this issue). The age relations with the adjacent units and features are complex. The deposit is clearly superposed on the Caloris basin material. The crater just to the west of the kidney-shaped depression appears embayed and thus predates the volcanism. To the northeast of the deposit, the central Caloris plains appear brighter and more mottled, are dominated by graben and wrinkle ridges (Murchie et al., 2008; Watters et al., 2009–this issue), and do not have the distinctive color characteristics of the deposit around the irregular depression. The contact between the Caloris interior plains and the edifice appears to be structural, with the boundary being characterized by a wrinkle-ridge-like scarp facing away from the Caloris interior and toward the edifice. Taken alone, these relationships could imply that the central Caloris plains were emplaced and deformed after the edifice, embaying it, and that this contact was then partly thrust over the base of the edifice. Alternatively, the edifice flows could be younger and have flowed down to, and been stopped by, an already existing wrinkle ridge. No other evidence is seen for the edifice or irregular depression deposits being cut by the tectonic ridges and rilles more common in the Caloris interior (Murchie et al., 2008; Watters et al., 2009–this issue).

Seven other occurrences of similar color anomalies, often associated with irregular depressions, are seen along the southern Caloris rim between these two examples (Figs. 4 and 5A–C). In color anomaly 2 (Fig. 5C), an irregular depression 25 km by 10 km lies at the northern end, and a 20-km-long arrow-shaped depression is at the southern end. An unusual 1–2-km-wide sinuous trough occurs just west and northwest of the anomaly and extends for about 100 km from the Caloris rim to the vicinity of the northern depression, where it is obscured by superposed craters. An elongate depression 2 km by 7 km

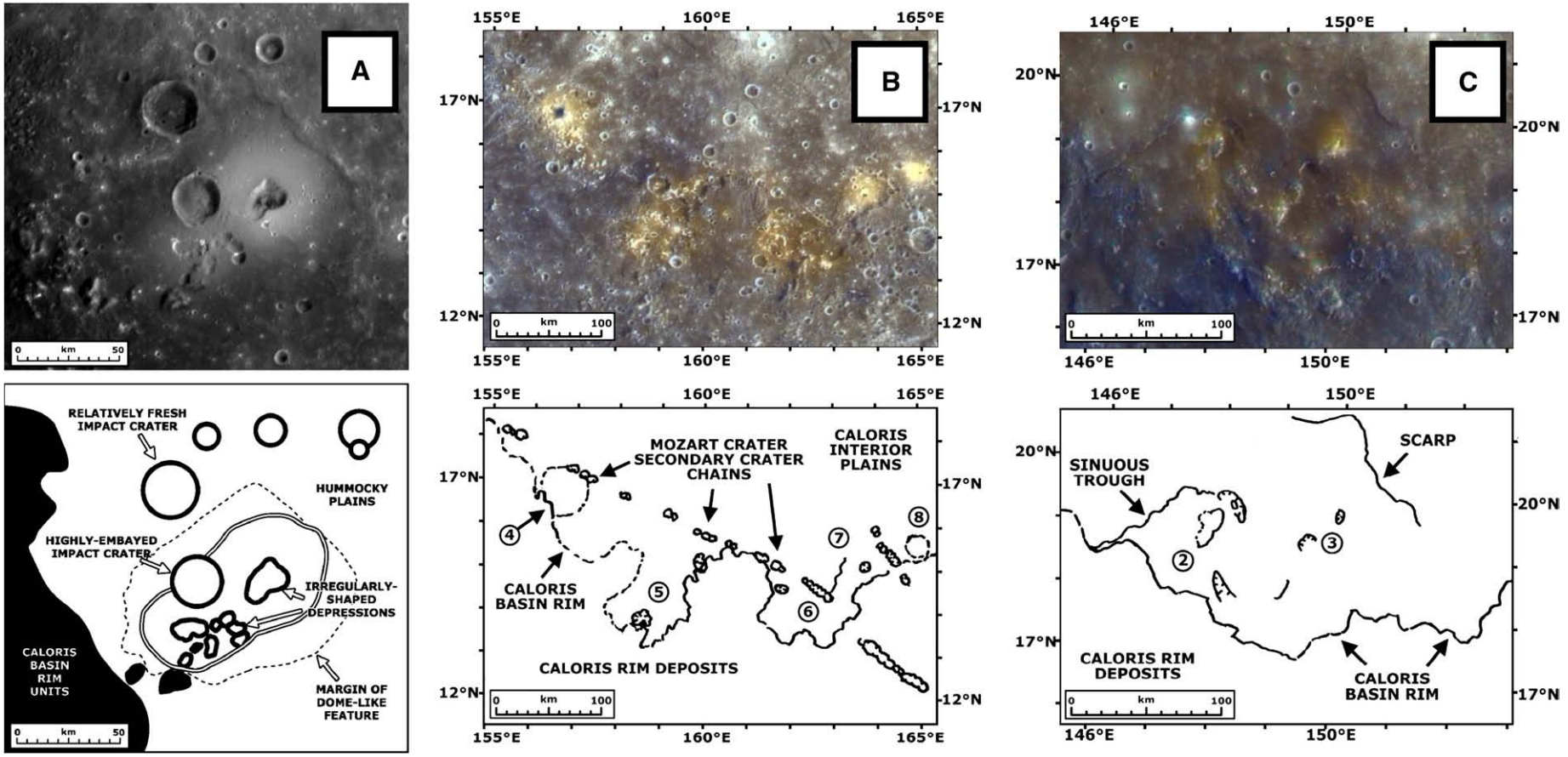

Fig. 5. (A) Westernmost rimless depression (occurrence 1) and surrounding deposits, including bright, diffuse deposits interpreted as a mantle formed by pyroclastic eruptions. (B) Color image and sketch map of rimless depression occurrences 2 and 3. (C) Color image and sketch map of rimless depression occurrences 4–8.

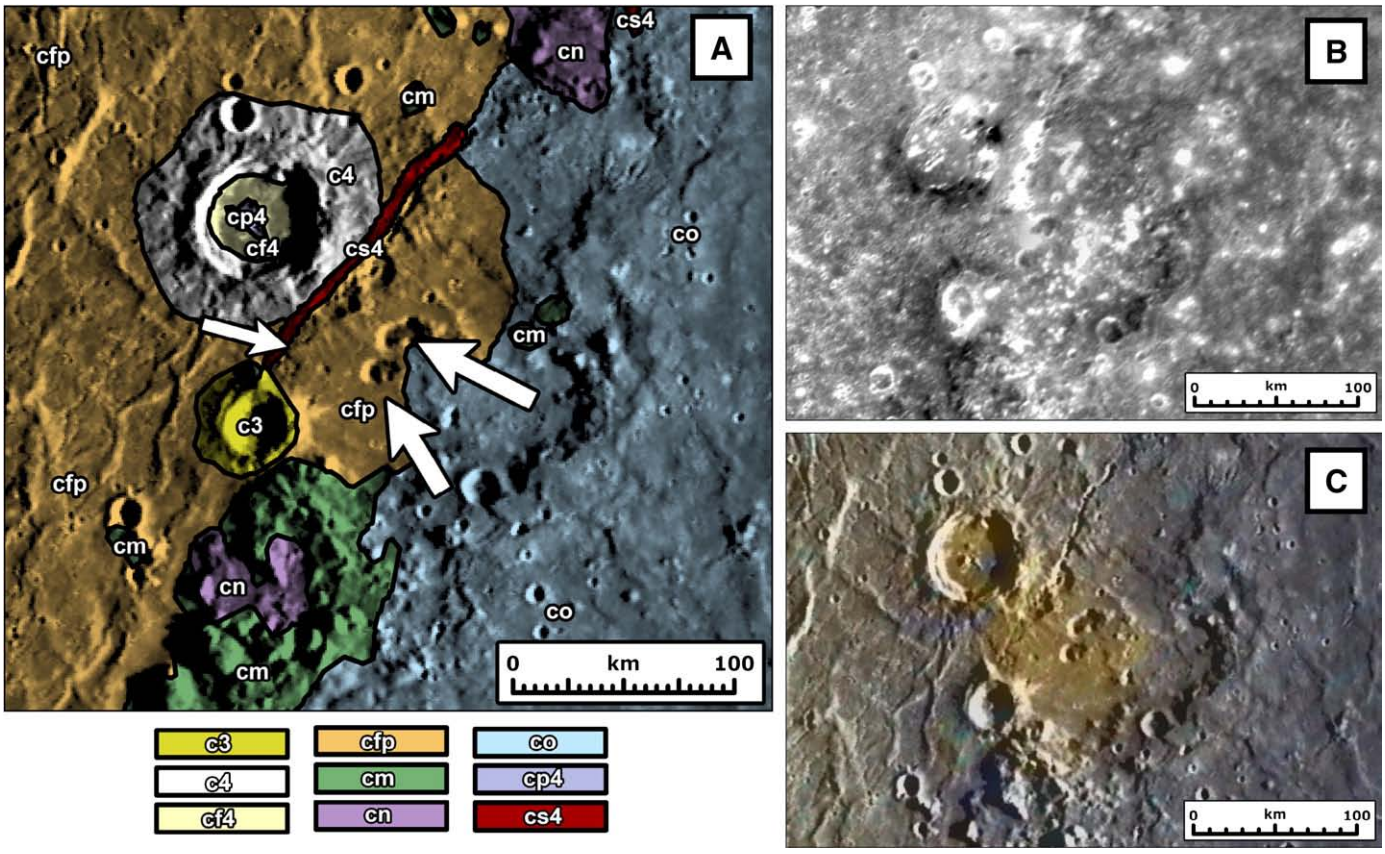

Fig. 6. (A) Geological map of the area surrounding rimless depression occurrence 9 (Guest and Greeley, 1983). (B, C) Images of rimless depression occurrence 9: (B) Mariner 10. (C) MESSENGER color images; red = inverse of PC2, green = PC1, and blue = relative visible color (430 nm/560 nm ratio) (Robinson et al., 2008; Blewett et al., 2009–this issue).

is centered on color anomaly 3, and a larger elongate depression (~12 km×7 km) is located about 18 km to the southwest; the southeast portion of this latter feature is incomplete and perhaps embayed. A distinctive sinuous scarp lies about 30 km to the northeast near the edge of the central Caloris plains unit; the scarp appears to be a wrinkle ridge or central plains flow front.

Color anomalies 4–8 occur along a 400-km-long swath of the southern Caloris basin interior (Figs. 4 and 5B), forming along both linear margins (4, 7, 8) and broad embayments in the basin rim (5, 6). The eastern part of this region is within ~200 km of the Mozart crater rim, located to the southeast. Several lines of Mozart secondary crater chains, up to about 10–12 km in diameter, trend southeast–northwest across the area. Most of the irregular depressions interpreted to be vents are readily distinguished from the linear crater chain clusters. Anomaly 4 is approximately circular with a diameter of ~50 km, a central dark feature, and a surrounding bright annulus ~5–8 km in width. The brightness and circularity suggests that this deposit might be in part pyroclastic in origin, similar to the interpretation of the bright diffuse annulus in area 1. Anomaly 5 contains a 15-km-long irregular rimless depression along its southern edge but not centrally located within the color anomaly; the setting of the depression, nestled in an embayment in the Caloris basin rim, is similar to the rimless depression in the lunar Orientale basin (Fig. 3). Anomaly 6 contains a small elongate depression about 10 km in length along its northern margin, but it is too close to a chain of Mozart secondaries of similar size to be certain of a non-impact origin. Area 7 shows a near-circular depression at the center of the ~50–60-km-wide anomaly, and area 8, ~20 km in diameter, is also bright and diffuse.

An interesting characteristic of this region (Fig. 4B, arrow) is that a similar color anomaly is associated with a ~19-km-diameter crater in the Caloris interior plains, about 180 km north of anomalies 7 and 8. If the rim and ejecta consist of excavated material similar to the deposits to the south, depth of excavation estimates suggest that deposits similar to those along the margin of the basin lie at depths of ~1–2 km below the central Caloris fill (Murchie et al., 2008; Watters et al., 2009–this issue). Spectral characteristics of the much larger crater about 160 km to the north indicate that deeper Caloris material is different in mineralogy (Murchie et al., 2008; Blewett et al., 2009–this issue; Watters et al., 2009–this issue).

In summary, the irregular rimless depressions associated with these color anomalies suggest that the related units can represent effusive volcanic deposits that sometimes build low shields and that also include pyroclastic eruptive contributions (Robinson and Lucey, 1997; see also Kerber et al., 2009–this issue). The materials have a high reflectance, are relatively reddish, and differ spectrally from the plains of the Caloris floor and other crustal material (Robinson et al., 2008; Murchie et al., 2008; Blewett et al., 2009–this issue). Although hints of sinuous rilles (Carr, 1974) are seen, these data are below the limits of resolution required to confidently interpret their nature and origin (e.g., Milkovich et al., 2002). The age of these deposits (younger or older than the Caloris interior regional plains) is ambiguous in many individual cases, but the stratigraphic relationships with superposed craters and color data suggest that they generally predate the Caloris interior plains (see also Murchie et al., 2008; Watters et al., 2009–this issue). Similar relationships are common on the Moon (Fig. 3), where early filling of basins can occur along the base of the massifs at the basin edge (e.g., Head, 1974a) and then these vents can be preserved as the basin interior fills with lavas and undergoes loading, flexure, and continued filling concentrated in the interior (Solomon and Head, 1979, 1980). Other spectrally distinctive edifices interpreted to be of effusive and explosive origin (the Gruithuisen and Mairan "red spots") are also

seen around the margin of the lunar Imbrium basin and date to early phases of the filling of the basin by volcanism (e.g., Head and McCord, 1978; Chevrel et al., 1999; Wagner et al., 2002). The loading and flexure associated with lava filling can, moreover, create stresses that are favorable to marginal dike emplacement and extrusion (e.g., Solomon and Head, 1980). Analysis of higher-spatial resolution data from the MESSENGER orbital phase will help to document further these deposits and to resolve these outstanding questions.

3. Evidence for volcanic filling of the Caloris basin interior

As exemplified by the Orientale basin, initially formed lunar impact basins are relatively deep and not filled with lava (Head, 1974b). Subsequent filling with mare basalts then covered and modified impact basin interiors and exteriors to a great degree, resulting in a series of stages of modification and loss of interior rings and structures (Head, 1982). For example, the lunar Imbrium basin is heavily modified and has been flooded out to the main topographic rim and beyond, largely obscuring the original basin ring structure (Fig. 7A). Comparison of the Imbrium basin and the Caloris basin (Fig. 7) shows that Caloris has been similarly filled nearly to the rim. Furthermore, many of the impact craters in the Imbrium interior (e.g., Archimedes; Head, 1982) show evidence for impact into the substrate, excavation of subsurface lavas, and then subsequent mare emplacement both embaying the exterior and flooding the interior (Fig. 7B, arrow). These relationships have been used to document the sequence of major units in the volcanic filling of the Caloris basin (Robinson et al., 2008; Murchie et al., 2008; Watters et al., 2009–this issue).

A major question in basin characterization is the role of impact melting and the abundance and areal significance of these deposits. On the Moon, impact melt deposits line the floor and interior of fresh basins (such as Orientale) that have not been subsequently filled extensively with lava (e.g., Head, 1974b; Howard et al., 1974; Spudis, 1993). The majority of lunar basins, however, have been subsequently filled with mare basalts (e.g., Hiesinger et al., 2000, 2003), and one might infer that if the basin appears filled, and the original basin rings buried and obscured, the original deposit of impact melt has been covered by subsequent lava flooding. Calculations strongly suggest, however, that impact melt is proportionally more important in larger basins (Cintala and Grieve, 1998) and at higher impact velocity (Cintala, 1992), specifically that the volume of impact melt formed relative to that of the crater will grow, and proportionally more will be retained inside the basin rim (Cintala and Grieve, 1998; Pierazzo et al., 2007). Given the higher mean impact velocity on Mercury and the

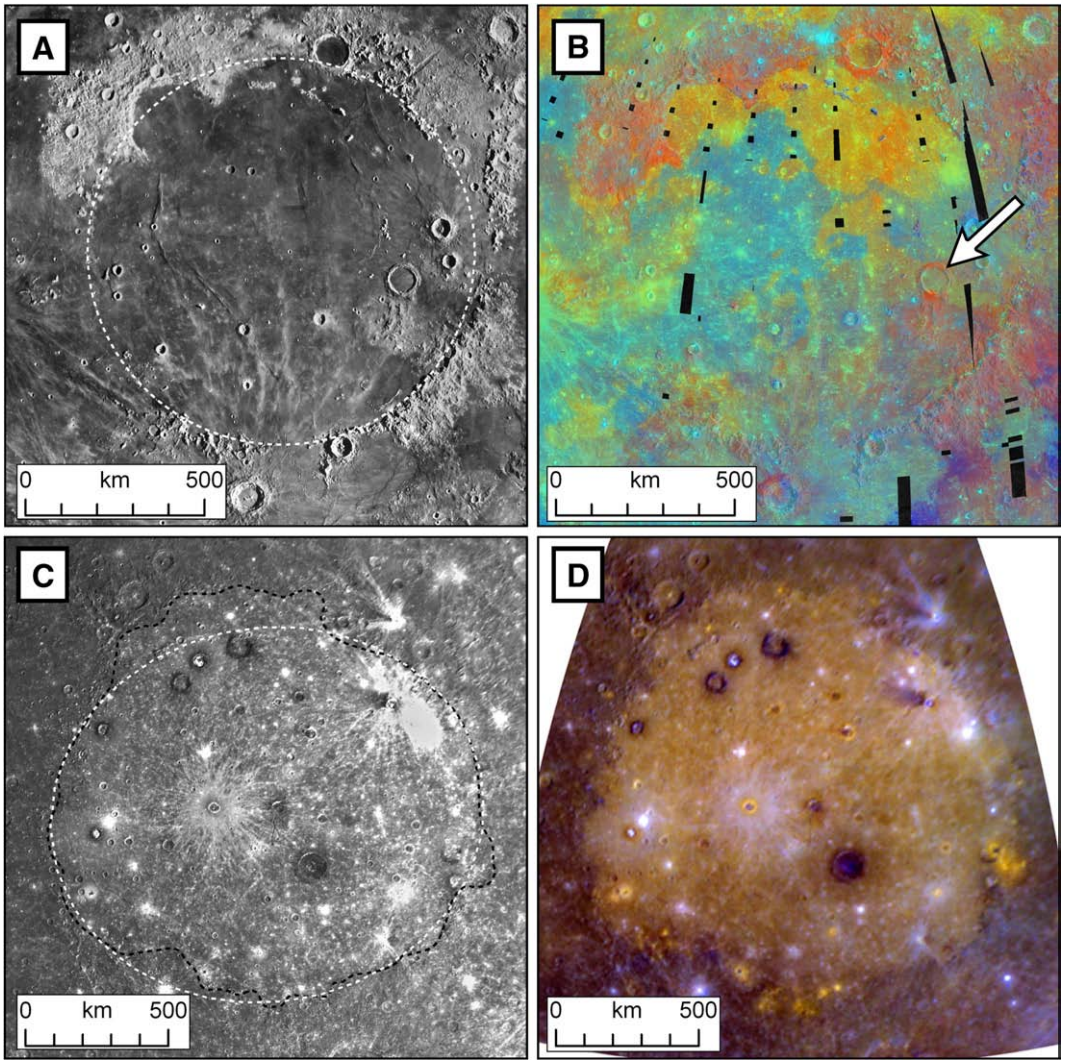

Fig. 7. Comparison of the lunar Imbrium basin and the Caloris basin on Mercury. (A) Earth-based telescopic view of the Imbrium basin on the Moon. Consolidated Lunar Atlas (Kuiper et al., 1967). (B) Color-composite Clementine image of the Imbrium basin (red: 750 nm/415 nm; green, 750 nm/950 nm; blue, 415 nm/750 nm). The crater Archimedes, which formed after the basin but was subsequently externally embayed and internally filled by lava, is shown by the arrow. (C) MESSENGER NAC mosaic of the Caloris basin. (D) MESSENGER WAC false-color image of the Caloris basin (see explanation in Fig. 4 caption).

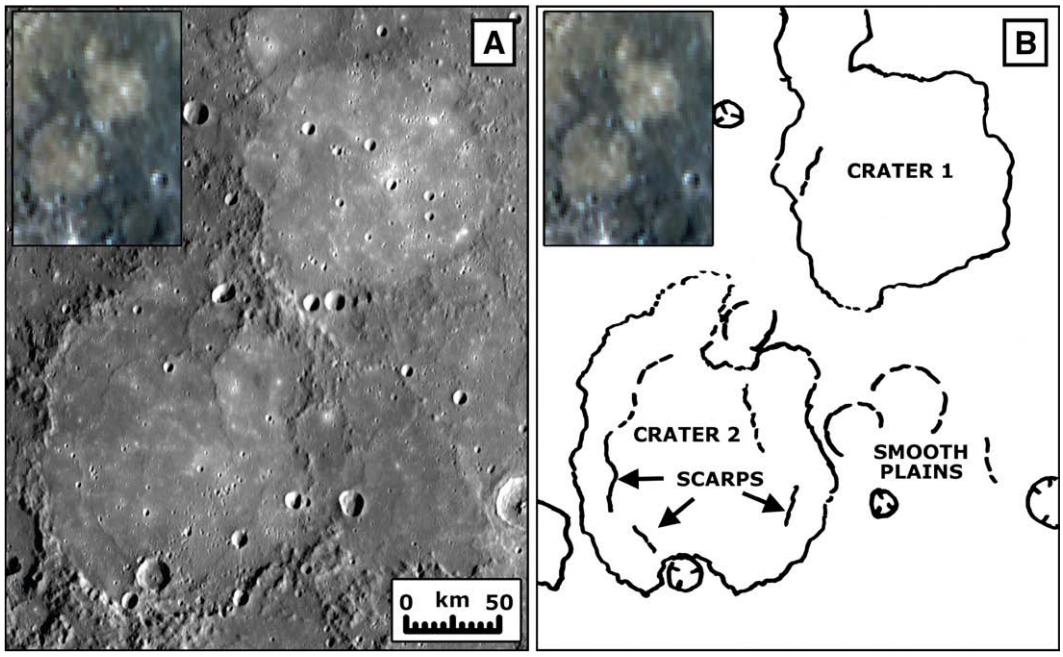

Fig. 8. Proximal smooth plains facies. High-albedo plains (image centered at 47.2°N, 121.1°E) are observed within the confines of ancient craters to the northwest of Caloris basin. (A) Mosaic of four MESSENGER NAC images (inset: WAC false-color image constructed from images taken with filters at 480, 750, and 1000 nm). (B) Sketch map of (A). Inset is identical to that of (A).

large size of the Caloris basin (~1550 km diameter), one must consider the possibility that the basin might have been filled primarily with impact melt. Examination of the Caloris basin interior (Figs. 4A and 7C–D) shows that this is unlikely to have been the case. The presence of marginal volcanic vents (Head et al., 2008), the distinctive color properties of the basin interior (Robinson et al., 2008), the evidence for volcanic fill from embayment and flooding relationships in superposed impact craters (Murchie et al., 2008; Watters et al., 2009–this issue), as well as differences in crater size-frequency distributions between the interior plains (Strom et al., 2008) and of the basin itself (Spudis and Guest, 1988; Table 3) all point to an origin of the interior Caloris plains by volcanic filling processes.

Despite many similarities, the surface mineralogy and diversity of the lava fill differs considerably between Imbrium and Caloris (Fig. 7). MESSENGER data from the first Mercury flyby were of insufficient resolution and illumination geometry to document the morphologic features that might reveal sequential emplacement of plains units over time, and the prominent color contrasts between volcanic units within Imbrium (see Hiesinger et al., 2000, 2003) are not observed in Caloris (Murchie et al., 2008; Robinson et al., 2008). Thus, a major goal for MESSENGER orbital operations will be the acquisition of imaging and spectral data to characterize and date the range of volcanic units in the interior.

4. Evidence for the role of volcanism in the emplacement of smooth plains exterior to the Caloris basin

The major units interpreted to be the deposits associated with the formation of the ~1550-km-diameter Caloris impact basin were defined by McCauley et al. (1981) as the Caloris Group and are summarized in Spudis and Guest (1988): mountain material (Caloris Montes Formation), intermontane plains (Nervo Formation), hummocky plains (Odin Formation), and lineated plains (Van Eyck Formation). A major question posed by the Mariner 10 results was an impact versus volcanic origin of smooth plains exterior to the Caloris basin (Fig. 1) (e.g., Murray, 1975; Strom et al., 1975; Wilhelms, 1976). Reprocessing of the Mariner 10 color data (Robinson and Lucey, 1997) provided compelling spectral, geologic, and stratigraphic evidence that some of the smooth plains were indeed of volcanic origin. Data from the first MESSENGER flyby help to support and confirm the findings of Robinson and Lucey (1997) and show that volcanism did indeed play an important role in the resurfacing of Mercury. MESSENGER images provide a basis for assessing the extent to which Cayley-like smooth plains of impact origin are present in the circum-Caloris region (e.g., Wilhelms, 1976). We examine evidence for exterior plains occurring proximal to the basin rim crest (defined as within a basin radius of the rim crest) and distal plains (defined as those more than a basin diameter from the rim crest).

4.1. Proximal plains deposits

Among plains deposits external to the Caloris basin but within a basin radius of the rim (Fig. 1), the MESSENGER albedo and color data reveal evidence for the embayment and filling of a Caloris radial structure and several large adjacent craters (Fig. 8, and inset), in a manner similar to the types of relationships seen in the reprocessed Mariner 10 data by Robinson and Lucey (1997). In this region, located several hundred kilometers northwest of the Caloris basin rim, a portion of the lineated Van Eyck Formation is buried by higher-albedo plains, forming a long linear swath extending away from the basin for ~375 km (Fassett et al., 2009–this issue). In surrounding areas, the background hummocky and knobby terrain and some smooth plains show morphological characteristics typical of the Odin Formation, and spectral characteristics of complex mixtures of low-reflectance material (LRM) and intermediate terrain (IT), typical of much of the circum-Caloris region (see southeastern part of Fig. 8) (Robinson et al., 2008; Blewett et al., 2009–this issue). Within this area, however, two ancient and highly degraded craters show evidence for higher-albedo surface deposits with distinctive spectral properties relative to the surroundings and interpreted by Robinson et al. (2008, their Fig. 1C) to be volcanic in origin. The southern crater (2), ~180 km in diameter, contains higher-albedo (due, in part, to superposed secondary craters), spectrally distinct plains units that differ from the adjacent smooth plains and hummocky material. The current data are of sufficient resolution to permit distinguishing units with color data (e.g., showing that they are different) but not to characterize them

(e.g., showing why they are different in detail) (see discussion in Head et al., 1978). The unit on the floor of crater 2 embays the interior crater margins, scarps are seen along the western margin, and scarps (most likely wrinkle ridges and/or flow fronts) are seen on the plains surface. Similar relationships are seen in the northern crater (1), ~125 km in diameter. These relationships (albedo and spectral distinctiveness, embayment relationships, and texture) provide stratigraphic evidence that support a volcanic origin for at least some of the proximal circum-Caloris smooth plains (see also Robinson et al., 2008).

4.2. Distal plains deposits

An occurrence of relatively high albedo and spectrally distinct regional smooth plains (centered at 4.5°S, 112°E) over 1500 km southwest of the Caloris basin rim (Fig. 9A and inset) is seen in the new data in an area of embayed and partly to largely filled ancient craters and basins near the terminator. In the southeastern part of this area (Fig. 9B), regional smooth plains fill an ancient basin over 300 km in diameter, and to the northwest, several large craters are partly or wholly filled by plains. The plains units delineated in Fig. 9A (see inset) show MDIS color characteristics indicating that they differ from the surrounding crater rims and uplands (Robinson et al., 2008); the color boundaries correspond to the margins of the plains mapped in Fig. 9B, supporting a volcanic origin for the plains, as also suggested from similar relationships in other areas in Mariner 10 data by Robinson and Lucey (1997). For example, the interior of a large ~145-km-diameter crater in the northwest has been completely modified by plains (Fig. 9C) (McClintock et al., 2008; their Fig. 2). We further analyzed these plains units using three approaches to assess their origin and emplacement histories: (1) the morphology of plains surfaces and the nature of plains boundaries, (2) the comparative size-frequency distribution of superposed and buried craters, and (3) the amount of fill implied by the depth of plains within craters.

The plains units have smooth surfaces that are distinct from the surrounding rougher, hummocky terrain. No evidence was observed for the types of volcanic vents seen around the outer margins of the Caloris basin rim (Head et al., 2008; Murchie et al., 2008). The majority of the plains are confined within craters and basins larger than 50 km across, and in adjacent intercrater regions. In some areas the outer boundary of the plains unit is marked by lobate scarps that appear to be superposed on the adjacent rough terrain (Fig. 10A). Similar marginal lobes seen in Mariner 10 data have been interpreted to represent the margins of lava flows that had yield strengths in the range of basaltic lavas on Earth (Wilson and Head, 2008); if such flows are cooling-limited, implied eruption rates would be in the range of the largest basalt fissure eruptions on Earth (Wilson and Head, 1981). Additional evidence for embayment and flooding relationships is seen in the form of partially buried craters common throughout the plains (Fig. 10B). Although no candidate volcanic vent features (e.g., sinuous rilles, domes) have yet been identified in these plains, the distinctive color differences (Fig. 9A, inset), the presence of lobate features along the edge of the plains units (Fig. 10A), and the clearly buried impact craters (Fig. 10B), are all consistent with a volcanic origin. We now use these relationships to assess the thickness of the plains.

Impact crater size-frequency distribution data provide important information about plains emplacement and thickness. In order to assess further the plains emplacement history, we analyzed the nature and distribution of impact craters in the five plains areas outlined in Fig. 9A and B. We counted craters in these regions and subdivided

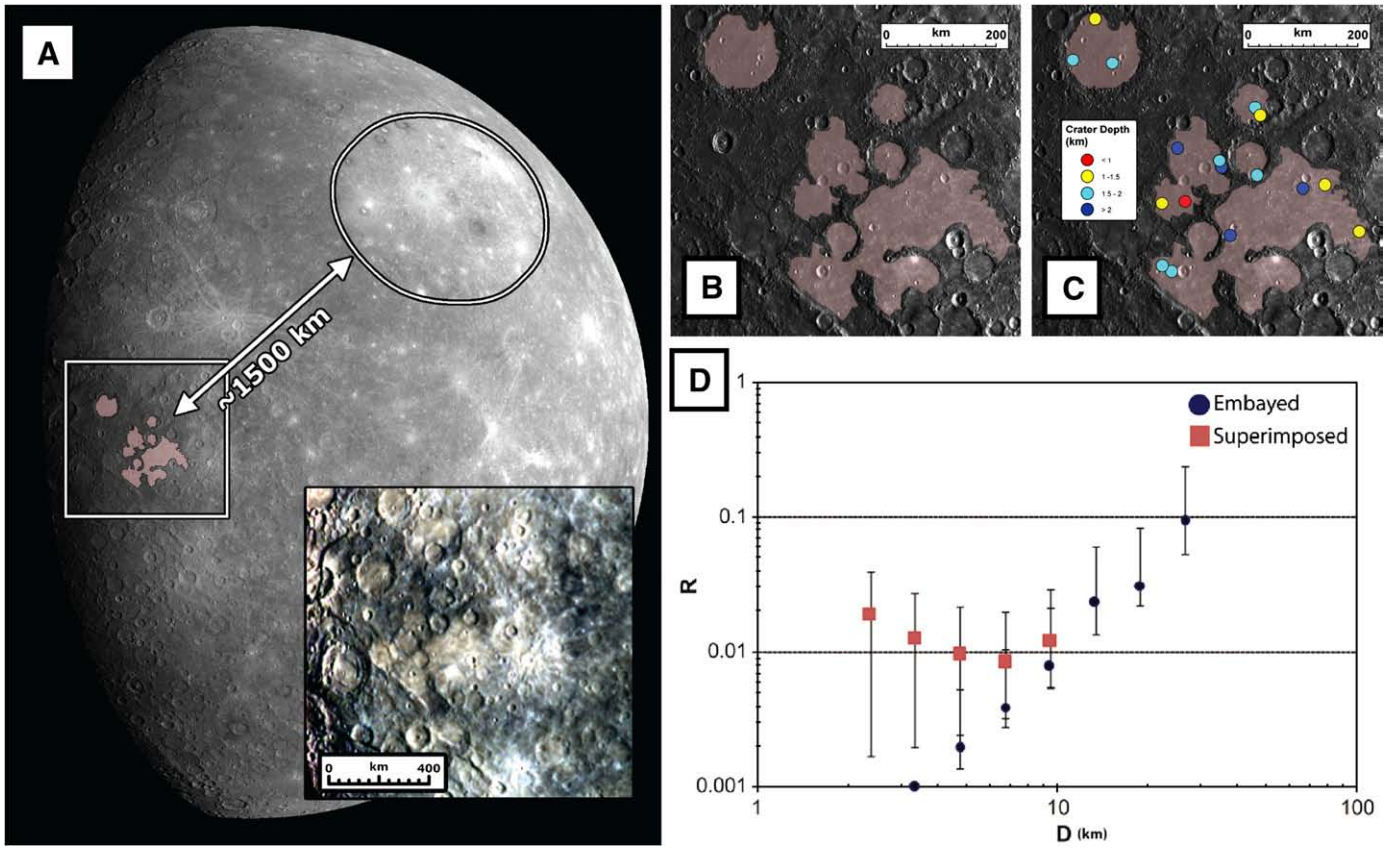

Fig. 9. Distal smooth plains facies. (A) High-albedo plains material is observed in MESSENGER WAC false-color images approximately 1500 km from the Caloris basin rim. Inset is derived from images with filters at 480, 750, and 1000 nm. (B) Detailed mapping of relatively high-albedo units from false-color WAC image. (C) Mapping of craters interpreted to be embayed or flooded by smooth plains material. Depth measurements are inferred from buried craters and depth/diameter relationships for fresh craters on Mercury (Pike, 1988). (D) Impact crater size-frequency distributions for superimposed and embayed craters within units mapped in (B) (see discussion in Strom et al., 2008, for explanation of *R* plots).

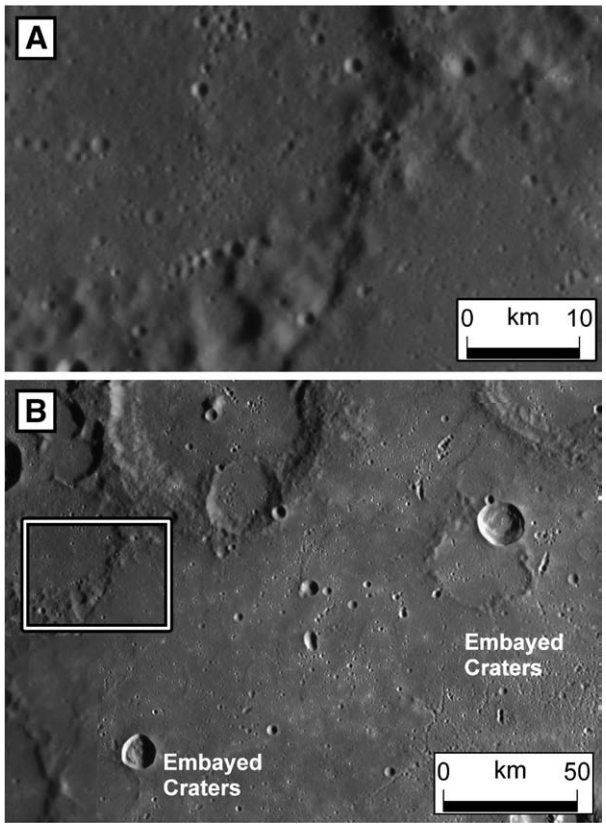

Fig. 10. Structures associated with distal smooth plains on Mercury. (A) Lobate scarp interpreted to be lava flow front. Image is a mosaic of MESSENGER NAC images. (B) Context for (A) and impact craters at several stages of embayment and internal filling.

them into those that were infilled or partially buried by the plains from those that were superposed on top of the plains. Comparison of the size-frequency distribution of the two populations shows that there is a steep falloff in the number of buried craters less than 10 km in diameter (Fig. 9D). We attribute this trend to the burial of older craters in this diameter range by the emplacement of smooth plains (e.g., Hiesinger et al., 2002). Fresh craters 10 km in diameter have rim heights above the surrounding target terrain of ~440 m (Pike, 1988); if the interpretation is correct that this deficiency of craters less than 10 km in diameter is due to flooding of fresh craters, then plains thicknesses of ~0.5 km or more would be required to completely flood them.

These thickness values for the plains units can also be compared with those derived from depth–diameter relationships for fresh craters. The current depths of impact craters that have been substantially filled with plains can be used to estimate the thickness of the fill by comparing these depths to the depths of fresh, unfilled craters (e.g., De Hon, 1979; see Head, 1982, for further discussion of the use and limitations of this method). Although detailed altimetry data are not yet available for these areas, we chose craters that were generally filled to very near the rim crest and used their diameter D together with empirically derived depth–diameter ratios calculated from Mariner 10 data by Pike (1988) to estimate depths. Four classes of craters are present in this embayed crater population, ranging from simple ($D<3$ km) to complex ($D>30$ km), giving a total of 15 craters that were measured (Fig. 9C). The greatest thickness for the plains derived from this approach was ~2 km (blue dots in Fig. 9C), and the smallest was ~0.5–1 km (red-orange dots in Fig. 9C), with an average depth of ~1.6 km. This average thickness, spread evenly over the whole area of plains counted (Fig. 9C), would yield a total volume of ~1.1×10^5 km^3, an order of magnitude lower than the Deccan Flood basalts (e.g., Widdowson et al., 1997) and somewhat larger than volumes associated with many smaller lunar maria (Head and Wilson, 1992; Yingst and Head, 1997, 1998, 1999). The assumption of fresh crater rim heights yields average thicknesses of less than a kilometer for the plains, more similar to the thicknesses and volumes for the small lunar maria (Yingst and Head, 1997, 1999). In summary, several lines of evidence from MESSENGER data support a volcanic origin for selected regions of smooth plains on Mercury (Spudis and Guest, 1988) and suggest that thickness of these deposits may range from several hundred meters up to as much as 1–2 km, comparable to those of many lunar maria (Head and Wilson, 1992).

In contrast to the local occurrences of spectrally distinctive areas described above, MDIS color data from the first MESSENGER flyby provide evidence that large areas of the deposits surrounding and proximal to the Caloris basin rim (including occurrences of the hummocky plains of the Odin Formation) are spectrally similar to each other (Robinson et al., 2008; Blewett et al., 2009–this issue). Furthermore, crater densities on the broad smooth plains regions proximal to the Caloris rim, and on parts of the Odin Formation, are considerably below those on the interior plains of Caloris (Strom et al., 2008). These relationships suggest that these units are unlikely to be Cayley-like ponded ejecta deposits (they are younger than the basin fill), and that at least some of the units interpreted to be related to the emplacement of Caloris basin ejecta (such as the Odin Formation; McCauley et al., 1981; Spudis and Guest, 1988) may instead be volcanically resurfaced or of volcanic origin. Further analysis of MDIS color data and more detailed crater size-frequency distribution studies are needed to: (1) map additional exterior deposits (Figs. 8 and 9) that are spectrally distinctive from the typical background material (e.g., Robinson et al., 2008; Blewett et al., 2009–this issue) and (2) assess the nature and origin of units that traditionally have been interpreted to be Caloris ejecta.

5. Additional criteria for recognition of volcanic plains: sequential fill and intermediate events

Impact craters provide templates for the analysis of landform degradation processes in space and time. Fresh impact craters and basins show systematic and characteristic changes in their morphologies as a function of increasing diameter, and this sequence has been well documented on the terrestrial planets, including Mercury (Pike, 1988). Degradation processes operating on impact craters on airless bodies, such as the Moon and Mercury, are dominated by three major factors. First, subsequent impacts at all scales tend to obliterate, partially bury, subdue, or soften the initial crater morphology. Second, tectonic deformation can deform the initial shape and shorten or extend the crater through brittle deformation processes, producing graben or ridges and scarps. Third, volcanic processes emplace lavas that can embay and flood crater interiors and exteriors, eventually completely burying them, and produce pyroclastic eruptions that can mantle and obscure crater morphology (Head, 1974a, 1975, 1976; Sharpton and Head, 1988).

Here we use new data acquired during the first MESSENGER flyby to examine a series of impact craters and basins that illustrate the transition from fresh crater morphology to completely buried craters now represented only by a deformed ring at the position of a buried crater rim. The major characteristics of fresh complex crater morphology (Pike, 1988) are illustrated in Fig. 11A. These include, from the interior outward, (1) central peaks or peak rings, (2) a flat crater floor with primary crater floor roughness, and (3) a terraced crater wall with ponds of impact melt on the back slopes of listric faults that formed the terraces during initial collapse of the transient cavity. From the rim crest outward, the morphologic elements include (1) a crater rim formed from structural uplift and crater ejecta (which decrease in height and thickness, respectively, with radial range,

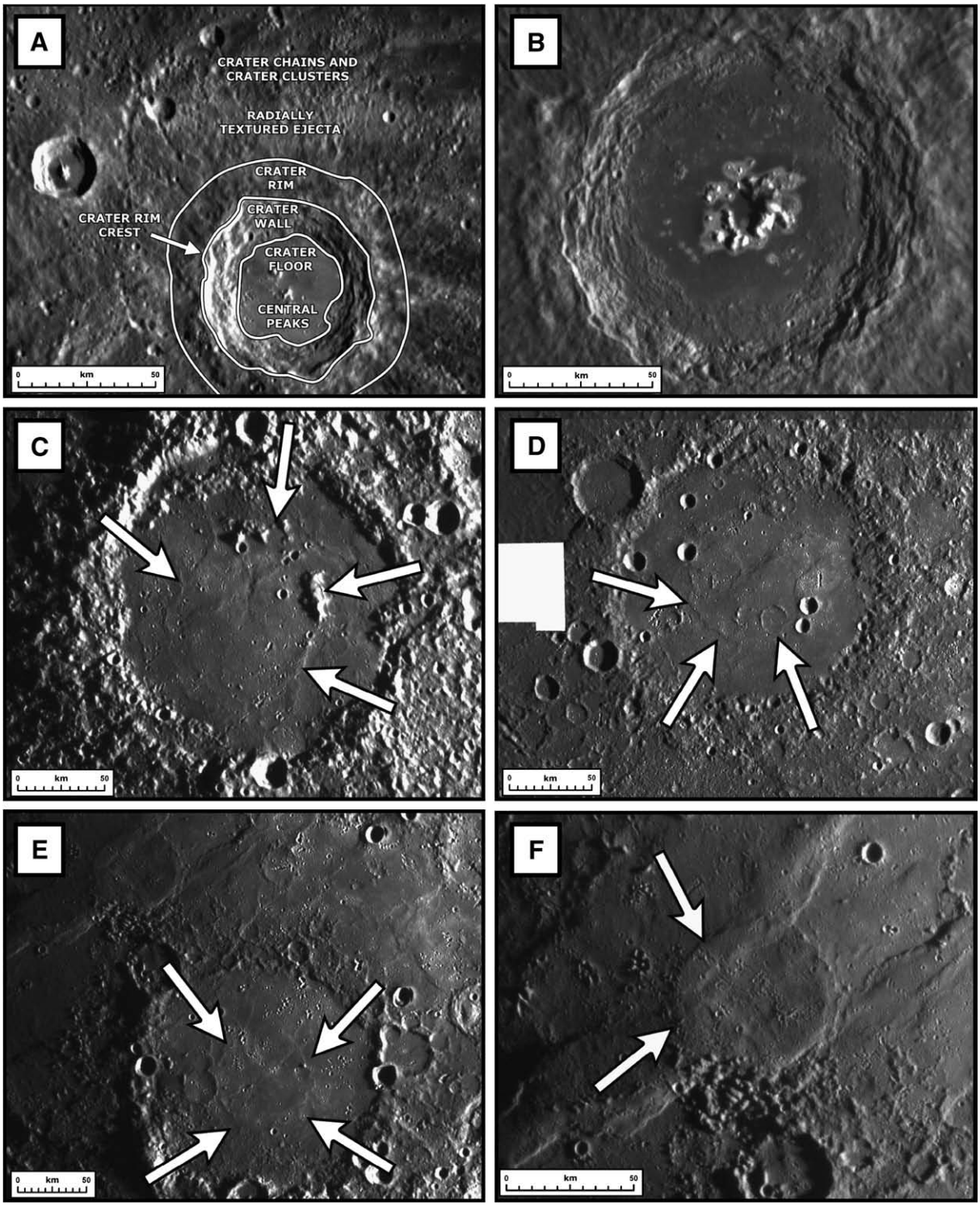

Fig. 11. Sequence of increasingly flooded craters and small basins. All panels are mosaics of MESSENGER NAC images. (A) Fresh crater structure and morphology observed in a ~60-km-diameter crater crater centered at 9.6°N, 125.7°E. (B) ~120-km-diameter Eminescu crater centered at 10.9°N, 114.2°E. (C) ~180-km-diameter crater centered at 21.9°N, 100.9°E. (D) ~165-km-diameter crater centered at 1.6°S, 106.9°E. (E) ~180-km-diameter crater centered at 6.5°N, 100.3°E. (F) ~60-km-diameter buried crater centered at 10.0°N, 98.2°E. Arrows in C–F show locations of buried rings and rims.

providing the characteristic outward-sloping topography of the crater rim), and (2) a radially textured ejecta deposit giving way outward to crater chains and crater clusters. These elements provide the template from which degradation processes can be measured.

A very fresh crater (Eminescu) interior, with an incipient peak ring, provides a starting example (Fig. 11B); primary roughness is still observed on the outer margins of the crater floor, and relatively low-albedo material surrounds and embays the flanks of the central peaks and the more prominent elements of the primary floor roughness. The smooth material could represent initial stages of volcanic flooding, but without more definitive evidence, it is not possible to distinguish it from impact melt deposits associated with initial crater formation. For example, the lunar crater Copernicus shows evidence for smooth deposits on the northwestern crater floor that are associated with impact melt emplacement (Pinet et al., 1993; Pieters et al., 1994).

Increasing levels of degradation and flooding are seen in Fig. 11C, in which the radial texture of the rim deposits is seen to be degraded but still visible (lower right), but the crater interior has been highly modified. The primary crater floor roughness has been replaced by smooth plains with wrinkle ridges and lobate scarps, and the plains clearly have flooded and buried the crater wall terraces over almost the entire crater interior, implying a significant depth of flooding. Also consistent with significant flooding is the nature of the remnant central peak ring. On the eastern and northern interior, remnants of a peak ring are still exposed, while in several other places along a circle extrapolated from the exposed peaks (see arrows), arcuate wrinkle-ridge structures suggest deformation concentrated above an underlying portion of the peak ring, as is often seen in lunar and martian craters and basins. No evidence is observed for the type of superposed lineated crater rim texture that would represent the influence of large basin secondary ejecta and the emplacement of Cayley-plains-type ejecta filling (e.g., Fassett et al., 2009–this issue), as observed in the circum-Imbrium basin region of the Moon.

A larger crater, ~165 km in diameter, appears even more completely flooded (Fig. 11D). The interior of the crater is filled with smooth plains, and no remnants of wall terraces are preserved; along the northwestern margin, the smooth plains almost breach the rim crest. In the interior, no primary remnants of a peak ring are preserved, although they are invariably present in fresh basins at this diameter (Pike, 1988). Instead, a semi-continuous wrinkle ridge ring is observed (see arrows) at the approximate location of the predicted peak ring (Pike, 1988). In addition, at least two superposed and flooded impact crater remnants are observed on the crater floor. The westernmost is ~32 km in diameter and almost completely flooded to its rim crest. The other, to the southwest, is smaller (~18 km in diameter); its southeastern rim is breached and flooded. Assuming that these craters were fresh when flooded, their rim crest diameters imply original depths of 2.0 and 1.7 km, respectively, and rim crests of ~800 and 600 m above the original surrounding terrain, respectively (Pike, 1988).

Another example similar in size (~180 km diameter; Fig. 11E) appears slightly more flooded. The interior plains flood nearly to the crater rim crest in the northern part of the crater, and a breached and nearly buried ~25-km-diameter impact crater is located on the western floor (suggesting interior fill to ~2 km and rim burial of ~700 m). There is a wrinkle-ridge ring in the interior at approximately the predicted ring position (Pike, 1988), with one knob at ~3 o'clock perhaps representing a high peak protruding from the buried peak ring. The larger crater itself (Fig. 11E) is also very highly degraded by individual superposed impacts; at least 14 craters larger than 10 km are superposed on the rim and rim crest. Several of these superposed craters have been flooded by smooth plains in their interiors, and the ejecta from these craters have been emplaced inside the large crater and subsequently embayed by smooth plains on the crater floor. For example, ejecta from the ~38-km-diameter crater on the northwestern rim landed inside the large crater, but the deposits are now flooded and embayed by smooth plains. Similarly, the exterior ejecta deposits of the large crater have been significantly embayed by surrounding smooth and intercrater plains, particularly to the north and northwest. Comparison of the crater rim texture to the north of the crater to that of a fresh crater (Fig. 11A) shows that the distal portions of the ejecta have been significantly embayed by plains. All evidence of distal radially textured deposits and secondary chains and clusters has been covered by smooth plains deposits, embaying the large crater to approximately the base of the raised rim (compare Fig. 11A and E).

As shown in these examples, and also illustrated in the analysis of the emplacement of smooth plains (Figs. 8 and 9), the rim crests of impact craters can be completely flooded and modified beyond any recognition of the primary landform, in a manner similar to the way in which peak rings have been flooded in these examples (Fig. 11C, D and E). For example, ~50 km to the northwest of the crater in Fig. 11E lies a wrinkle-ridge ring embedded in a pattern of generally northeast-trending linear wrinkle ridge segments (Fig. 11F). A few small peaks occur on the northeastern portion of the ring, perhaps representing the remnants of a flooded and buried rim crest.

Partially flooded and embayed craters and wrinkle-ridge rings are common in the lunar maria and in the regional plains of Mars, where they represent impact craters that have been partially or wholly buried by lava flows. In these cases, wrinkle ridges form from contractional deformation of the volcanic plains, and where there is subsurface topography, such as a flooded impact crater, the topography can act as a stress concentrator that localizes deformation of the near-surface material. In the case of the Letrone–Flamsteed region of southern Oceanus Procellarum on the Moon, the crater Letrone is embayed and modified, with its northern margin completely flooded (Whitford-Stark and Head, 1980; Mustard and Head, 1996), while farther to the north, the crater Flamsteed is almost completely buried by mare basalts (Pieters et al., 1980; Heather and Dunkin, 2002), forming an incipient wrinkle-ridge ring as part of the regional northwest–southeast-trending system in Oceanus Procellarum (Whitford-Stark and Head, 1980). The presence of wrinkle-ridge rings is generally interpreted to imply flooding of a crater to a level above its rim crest and subsequent deformation of the plains. The presence of wrinkle ridge rings can then be used to infer the emplacement of volcanic plains, and also to estimate the thicknesses of these plains from the size of the ring and the inferred diameter, depth, and rim height of the original crater (De Hon, 1979).

6. Discussion and conclusions

Observations made during the first MESSENGER flyby of Mercury have helped to address and resolve a series of questions, largely outstanding since the end of the Mariner 10 mission, related to the existence, nature, and distribution of volcanism on that planet. These new data have revealed numerous volcanic vents, in the form of irregularly shaped rimless depressions, located preferentially around the interior of the edge of the Caloris basin. These vents are interpreted to be sources for effusive volcanism, including a shield in excess of 100 km in diameter, and pyroclastic eruptions, represented by bright haloes around the vents that are distinctive in color data. The interior of the Caloris basin is filled with plains units spectrally distinct from the rim deposits, and comparison with the lunar Imbrium basin and superposed impact crater stratigraphy provide evidence that these units are volcanic in origin. Plains with distinctive color characteristics, lobate plains unit margins, and the sizes of embayed and buried impact craters all support the interpretation that at least some of the smooth plains surrounding the exterior of the Caloris basin (Fig. 1) are volcanic in origin. Other color and crater size–frequency distribution relationships suggest that large areas near the basin rim are unlikely to be Cayley-like ponded ejecta deposits (they are younger than the basin fill), and that at least some of the units interpreted to be related to the emplacement of Caloris basin ejecta (such as the Odin Formation; McCauley et al., 1981; Spudis and Guest, 1988) may instead be volcanically resurfaced or volcanic in origin. Large impact craters show a sequence of embayment of interior floor and exterior ejecta deposits that supports a volcanic origin for filling material. Flooding relationships documented in selected areas suggest volcanic plains thicknesses of many hundreds of meters and local thicknesses inside impact craters of up to several kilometers. In addition to the evidence for volcanic deposits outlined here, the first MESSENGER flyby revealed evidence for intrusive activity in the form of a floor-fractured crater, similar to some seen on the Moon (Schultz, 1976a), and a radial graben swarm centered in the Caloris basin (e.g., Murchie et al., 2008) that may have been formed by subsurface dike-emplacement events (e.g., Head et al., 2008).

These new data provide evidence that supports and confirms earlier hypotheses from Mariner 10 data that volcanism was

important in shaping the surface of Mercury (Strom et al., 1975; Spudis and Guest, 1988; Robinson and Lucey, 1997). The emerging picture of the volcanic style of Mercury is similar to that of the Moon, the solar system's other small one-plate terrestrial planetary body (Head and Wilson, 1991, 1992). There are no major shield volcanoes such as the Tharsis Montes on Mars, shallow magma reservoirs are rare, and there is little evidence of mantle hot spots as long-lived sites of magmatism and deformation. Also similar to the Moon is the evidence for linkage of volcanism and its distribution and style to the formation of impact basins (Head, 1976; Head and Wilson, 1992). In a manner similar to those on the Moon, volcanic vents are observed around the margins of impact basins, often in association with basin rings (Fig. 7), and the inner parts of the basin tend to be filled by younger volcanic deposits, embaying the older marginal deposits. Pyroclastic deposits are often associated with these volcanic vents and, because of their preservation as blankets around the margins, provide evidence of these earlier phases of basin-related volcanism. As with the Moon, the nature of these deposits can provide important information on mantle and crustal volatiles and chemistry (Saal et al., 2008; Kerber et al., 2009–this issue). Further, emerging evidence for exterior smooth plains of volcanic origin shows that their characteristics and distribution are very similar to those on the Moon; these involve embayment and filling of large impact craters to depths measured in hundreds of meters to over a kilometer (e.g., De Hon, 1979) and the formation of patches of plains deposits similar in scale to those on the Moon (e.g., Yingst and Head, 1997, 1998, 1999).

Upcoming MESSENGER flybys and orbital operations will provide the high spatial and spectral resolution needed to identify small-scale geological features diagnostic of volcanism, to distinguish units of different composition and mineralogy, and to determine the size-frequency distribution of impact craters on the scale of individual units. This array of information will permit a census of plains units of both impact and volcanic origin. Altimetry and gravity data will also provide quantitative information helpful to an assessment of the thicknesses, volumes, and deformation histories of both types of plains.

Acknowledgements

We gratefully acknowledge the personnel of the Johns Hopkins University Applied Physics Laboratory, who have planned and executed the MESSENGER mission. Without their dedication and perseverance, this analysis would not have been possible. We thank Kris Becker, Mark Robinson, Brett Denevi, and all those who worked long and hard to process and calibrate the MDIS data. The careful reviews by Mark Cintala and an unidentified reviewer helped to improve the manuscript and are gratefully acknowledged. The MESSENGER Project is supported by the NASA Discovery Program under contracts NASW-00002 to the Carnegie Institution of Washington and NAS5-97271 to the Johns Hopkins University Applied Physics Laboratory.

References

Blewett, D.T., Robinson, M.S., Denevi, B.W., Gillis-Davis, J.J., Head, J.W., Solomon, S.C., Holsclaw, G.M., McClintock, W.E., 2009. Multispectral imaging of Mercury from the first MESSENGER flyby: analysis of global and regional color trends. Earth Planet. Sci. Lett. 285, 272–282 (this issue).

Carr, M.H., 1966. Geologic map of the Mare Serenitatis region of the Moon. Map I-489, Misc. Investigations Ser., U.S. Geological Survey, Denver, Colo.

Carr, M.H., 1974. The role of lava erosion in the formation of lunar rilles and martian channels. Icarus 22, 1–23.

Chevrel, S.D., Pinet, P.C., Head, J.W., 1999. Gruithuisen domes region: a candidate for an extended non-mare volcanism unit on the Moon. J. Geophys. Res. 104, 16,515–16,529.

Cintala, M.J., 1992. Impact-induced thermal effects in the lunar and mercurian regoliths. J. Geophys. Res. 97, 947–973.

Cintala, M.J., Grieve, R.A.F., 1998. Scaling impact melting and crater dimensions: implications for the lunar cratering record. Meteorit. Planet. Sci. 33, 889–912.

Crumpler, L.S., Head, J.W., Aubele, J.C., 1996. Calderas on Mars: characteristics, structural evolution, and associated flank structures. In: McGuire, W.J., Jones, A.P., Neuberg, J. (Eds.), Volcano Instability on the Earth and Other Planets. Special Publication No. 110. Geological Society of London, pp. 307–347.

De Hon, R.A., 1979. Thickness of the western mare basalts. Proc. Lunar Planet. Sci. Conf. 10, 2935–2955.

De Hon, R.A., Scott, D.H., Underwood, Jr., J.R., 1981. Geologic map of the Kuiper quadrangle of Mercury (H-6). Map I-1233, Misc. Investigations Ser., U.S. Geological Survey, Denver, Colo.

Dzurisin, D., 1978. The tectonic and volcanic history of Mercury as inferred from studies of scarps, ridges, troughs, and other lineaments. J. Geophys. Res. 83, 4883–4906.

Fassett, C.I., Head, J.W., Blewett, D.T., Chapman, C.R., Dickson, J.L., Murchie, S.L., Solomon, S.C., Watters, T.R., 2009. Caloris impact basin: exterior geomorphology, stratigraphy, morphometry, radial sculpture, and smooth plains deposits. Earth Planet. Sci. Lett. 285, 297–308 (this issue).

Gaddis, L.R., Staid, M.I., Tyburczy, J.A., Hawke, B.R., Petro, N.E., 2003. Compositional analyses of lunar pyroclastic deposits. Icarus 161, 262–282.

Guest, J.E., Greeley, R., 1983. Geologic map of the Shakespeare quadrangle of Mercury (H-3). Map I-1408, Misc. Investigations Ser., U.S. Geological Survey, Denver, Colo.

Hawkins III, S.E., Boldt, J.D., Darlington, E.H., Espiritu, R., Gold, R.E., Gotwols, B., Grey, M.P., Hash, C.D., Hayes, J.R., Jaskulek, S.E., Kardian, C.J., Keller, M.R., Malaret, E.R., Murchie, S.L., Murphy, P.K., Peacock, K., Prockter, L.M., Reiter, R.A., Robinson, M.S., Schaefer, E.D., Shelton, R.G., Sterner II, R.E., Taylor, H.W., Watters, T.R., Williams, B.D., 2007. The Mercury Dual Imaging System on the MESSENGER spacecraft. Space Sci. Rev. 131, 247–338.

Head, J.W., 1974a. Lunar dark-mantle deposits: possible clues to the distribution of early mare deposits. Proc. Lunar Sci. Conf. 5, 207–222.

Head, J.W., 1974b. Orientale multi-ringed basin interior and implications for petrogenesis of the lunar samples. Moon 11, 327–356.

Head, J.W., 1975. Processes of lunar crater degradation: changes in style with geologic time. Moon 12, 299–329.

Head, J.W., 1976. Lunar volcanism in space and time. Rev. Geophys. Space Phys. 14, 265–300.

Head, J.W., 1982. Lava flooding of ancient planetary crusts: geometry, thickness, and volumes of flooded lunar impact basins. Moon Planets 26, 61–88.

Head, J.W., Gifford, A., 1980. Lunar mare domes: classification and modes of origin. Moon Planets 22, 235–258.

Head, J.W., McCord, T.B., 1978. Imbrian-age highland volcanism on the Moon: the Gruithuisen and Mairan domes. Science 199, 1433–1436.

Head, J.W., Wilson, L., 1979. Alphonsus-type dark-halo craters: morphology, morphometry, and eruption conditions. Proc. Lunar Planet. Sci. Conf. 10, 2861–2897.

Head, J.W., Wilson, L., 1991. Absence of large shield volcanoes and calderas on the Moon: consequence of magma transport phenomena? Geophys. Res. Lett. 18, 2121–2124.

Head, J.W., Wilson, L., 1992. Lunar mare volcanism: stratigraphy, eruption conditions, and the evolution of secondary crusts. Geochim. Cosmochim. Acta 55, 2155–2175.

Head, J.W., Wilson, L., 2001. Theoretical aspects of magma generation, ascent and eruption on Mercury and comparison with composition and morphology of surface features. Mercury: Space Environment, Surface, and Interior. Lunar and Planetary Institute, Houston, Tex. abstract 8039.

Head, J.W., Pieters, C.M., McCord, T., Adams, J., Zisk, S., 1978. Definition and detailed characterization of lunar surface units using remote observations. Icarus 33, 145–172.

Head, J.W., Wilson, L., Weitz, C.M., 2002. Dark ring in southwestern Orientale basin: origin as a single pyroclastic eruption. J. Geophys. Res. 107, 5001. doi:10.1029/2000JE001438.

Head, J.W., Chapman, C.R., Domingue, D.L., Hawkins III, S.E., McClintock, W.E., Murchie, S.L., Prockter, L.M., Robinson, M.S., Strom, R.G., Watters, T.R., 2007. The geology of Mercury: the view prior to the MESSENGER mission. Space Sci. Rev. 131, 41–84.

Head, J.W., Murchie, S.L., Prockter, L.M., Robinson, M.S., Solomon, S.C., Strom, R.G., Chapman, C.R., Watters, T.R., McClintock, W.E., Blewett, D.T., Gillis-Davis, J.J., 2008. Volcanism on Mercury: evidence from the first MESSENGER flyby. Science 321, 69–72.

Head, J.W., Murchie, S.L., Prockter, L.M., Solomon, S.C., Strom, R.G., Chapman, C.R., Watters, T.R., Blewett, D.T., Gillis-Davis, J.J., Fassett, C.I., Dickson, J.L., Hurwitz, D.M., Ostrach, L.R., 2009. Evidence for intrusive activity on Mercury from the first MESSENGER flyby. Earth Planet. Sci. Lett. 285, 251–262 (this issue).

Heather, D.J., Dunkin, S.K., 2002. A stratigraphic study of southern Oceanus Procellarum using Clementine multispectral data. Planet. Space Sci. 50, 1299–1309.

Hiesinger, H., Jaumann, R., Neukum, G., Head, J.W., 2000. Age of mare basalts on the lunar nearside. J. Geophys. Res. 105, 29,239–29,275.

Hiesinger, H., Head III, J.W., Wolf, U., Jaumann, R., Neukum, G., 2002. Lunar mare basalt flow units: thicknesses determined from crater size-frequency distributions. Geophys. Res. Lett. 29, 1248. doi:10.1029/2002GL014847.

Hiesinger, H., Head III, J.W., Wolf, U., Jaumann, R., Neukum, G., 2003. Ages and stratigraphy of mare basalts in Oceanus Procellarum, Mare Nubium, Mare Cognitum, and Mare Insularum. J. Geophys. Res. 108, 5065. doi:10.1029/2002JE001985.

Howard, K., Wilhelms, D., Scott, D., 1974. Lunar basin formation and highland stratigraphy. Rev. Geophys. 12, 309–327.

Kerber, L., Head, J.W., Solomon, S.C., Murchie, S.L., Blewett, D.T., Wilson, L., 2009. Explosive volcanic eruptions on Mercury: eruption conditions, magma volatile content, and implications for mantle volatile abundances. Earth Planet. Sci. Lett. 285, 263–271 (this issue).

King, J.S., Scott, D.H., 1990. Geologic map of the Beethoven quadrangle of Mercury (H-7). Map I-2048, Misc. Investigations Ser., U.S. Geological Survey, Denver, Colo.

Kuiper, G.P., Whitaker, E.A., Strom, R.G., Fountain, J.W., Larson, S.M., 1967. Consolidated Lunar Atlas. Contributions of the Lunar and Planetary Laboratory No. 4. Lunar and Planetary Laboratory, University of Arizona, Tucson, Ariz.

Lucchitta, B.K., Schmitt, H.H., 1974. Orange material in the Sulpicius Gallus Formation at the southwestern edge of Mare Serenitatis. Proc. Lunar Sci. Conf. 5, 223–234.
Malin, M.C., 1978. Surfaces of Mercury and the Moon: effects of resolution and lighting conditions on the discrimination of volcanic features. Proc. Lunar Planet. Sci. Conf. 9, 3395–3409.
McCauley, J.F., Guest, J.E., Schaber, G.G., Trask, N.J., Greeley, R., 1981. Stratigraphy of the Caloris basin, Mercury. Icarus 15, 363–367.
McClintock, W.E., Izenberg, N.R., Holsclaw, G.M., Blewett, D.T., Domingue, D.L., Head, J.W., Helbert, J., McCoy, T.J., Murchie, S.L., Robinson, M.S., Solomon, S.C., Sprague, A.L., Vilas, F., 2008. Spectroscopic observations of Mercury's surface reflectance during MESSENGER's first Mercury flyby. Science 321, 62–65.
McGill, G.E., King, E.E., 1983. Geologic map of the Victoria quadrangle of Mercury (H-2). Map I-1409, Misc. Investigations Ser., U.S. Geological Survey, Denver, Colo.
Milkovich, S.M., Head, J.W., Wilson, L., 2002. Identification of mercurian volcanism: resolution effects and implications for MESSENGER. Meteorit. Planet. Sci. 37, 1209–1222.
Murchie, S.L., Watters, T.R., Robinson, M.S., Head, J.W., Strom, R.G., Chapman, C.R., Solomon, S.C., McClintock, W.E., Prockter, L.M., Domingue, D.L., Blewett, D.T., 2008. Geology of the Caloris basin, Mercury: a view from MESSENGER. Science 321, 73–76.
Murray, B.C., 1975. The Mariner 10 pictures of Mercury: an overview. J. Geophys. Res. 80, 2342–2344.
Murray, B.C., Strom, R.G., Trask, N.J., Gault, D.E., 1975. Surface history of Mercury: implications for terrestrial planets. J. Geophys. Res. 80, 2508–2514.
Mustard, J.F., Head, J.W., 1996. Buried stratigraphic relationships along the south-western shores of Oceanus Procellarum: implications for early lunar volcanism. J. Geophys. Res. 101, 18,913–18,925.
Oberbeck, V.R., 1975. The role of ballistic erosion and sedimentation in lunar stratigraphy. Rev. Geophys. Space Phys. 13, 337–362.
Oberbeck, V.R., Morrison, R.H., Hörz, F., Quaide, W.L., 1974. Smooth plains and continuous deposits of craters and basins. Proc. Lunar Sci. Conf. 5, 111–136.
Oberbeck, V.R., Quaide, W.L., Arvidson, R.E., Aggarwal, H.R., 1977. Comparative studies of lunar, Martian, and Mercurian craters and plains. J. Geophys. Res. 82, 1681–1698.
Pierazzo, E., Vickery, A.M., Melosh, H.J., 2007. A reevaluation of impact melt production. Icarus 127, 408–423.
Pieters, C.M., Head, J.W., Adams, J.B., McCord, T.B., Zisk, S.H., Whitford-Stark, J.L., 1980. Late high titanium basalts of the western maria: geology of the Flamsteed region of Oceanus Procellarum. J. Geophys. Res. 85, 3913–3938.
Pieters, C.M., Staid, M.I., Fischer, E.M., Tompkins, S., He, G., 1994. A sharper view of impact craters from Clementine data. Science 266, 1844–1848.
Pike, R.J., 1988. Geomorphology of impact craters on Mercury. In: Vilas, F., Chapman, C.R., Matthews, M.S. (Eds.), Mercury. Univ. Arizona Press, Tucson, Ariz., pp. 165–273.
Pinet, P.C., Chevrel, S.D., Martin, P., 1993. Copernicus: a regional probe of the lunar interior. Science 260, 797–801.
Robinson, M.S., Lucey, P.G., 1997. Recalibrated Mariner 10 color mosaics: implications for mercurian volcanism. Science 275, 197–200.
Robinson, M.S., Murchie, S.L., Blewett, D.T., Domingue, D.L., Hawkins, S.E., Head, J.W., Holsclaw, G.M., McClintock, W.E., McCoy, T.J., McNutt, R.L., Prockter, L.M., Solomon, S.C., Watters, T.R., 2008. Reflectance and color variations on Mercury: indicators of regolith processes and compositional heterogeneity. Science 321, 66–69.
Saal, A.E., Hauri, E.H., Cascio, M.L., Van Orman, J.A., Rutherford, M.C., Cooper, R.F., 2008. Volatile content of lunar volcanic glasses and the presence of water in the Moon's interior. Nature 454, 192–195.
Schaber, G.G., McCauley, J.F., 1980. Geologic map of the Tolstoj quadrangle of Mercury (H-8). Map I-1199, Misc. Investigations Ser., U.S. Geological Survey, Denver, Colo.
Schultz, P.H., 1976a. Floor-fractured lunar craters. Moon 15, 241–273.
Schultz, P.H., 1976b. Moon Morphology: Interpretations based on Lunar Orbiter Photography. University of Texas Press, Austin, Tex. 604 pp.
Schultz, P.H., 1977. Endogenic modification of impact craters on Mercury. Phys. Earth Planet. Inter. 15, 202–219.
Sharpton, V.L., Head, J.W., 1988. Lunar mare ridges: analysis of ridge-crater intersections and implications for the tectonic origin of mare ridges. Proc. Lunar Planet. Sci. Conf. 18, 307–317.
Solomon, S.C., Head, J.W., 1979. Vertical movement in mare basins: relation to mare emplacement, basin tectonics, and lunar thermal history. J. Geophys. Res. 84, 1667–1682.
Solomon, S.C., Head, J.W., 1980. Lunar mascon basins: lava filling, tectonics, and evolution of the lithosphere. Rev. Geophys. Space Phys. 18, 107–141.
Solomon, S.C., McNutt Jr., R.L., Gold, R.E., Domingue, D.L., 2007. MESSENGER mission overview. Space Sci. Rev. 131, 3–39.
Solomon, S.C., McNutt, R.L., Watters, T.R., Lawrence, D.J., Feldman, W.C., Head, J.W., Krimigis, S.M., Murchie, S.L., Phillips, R.J., Slavin, J.A., Zuber, M.T., 2008. Return to Mercury: a global perspective on MESSENGER's first Mercury flyby. Science 321, 59–62.
Spudis, P.D., 1993. The Geology of Multi-Ring Impact Basins. Cambridge Univ. Press, Cambridge, UK. 263 pp.
Spudis, P.D., Guest, J.E., 1988. Stratigraphy and geologic history of Mercury. In: Vilas, F., Chapman, C.R., Matthews, M.S. (Eds.), Mercury. University of Arizona Press, Tucson, Ariz., pp. 118–164.
Spudis, P.D., Prosser, J.G., 1984. Geologic map of the Michelangelo quadrangle of Mercury (H-12). Map I-1659, Misc. Investigations Ser., U.S. Geological Survey, Denver, Colo.
Strom, R.G., 1977. Origin and relative age of lunar and mercurian intercrater plains. Phys. Earth Planet. Inter. 15, 156–172.
Strom, R.G., Trask, N.J., Guest, J.E., 1975. Tectonism and volcanism on Mercury. J. Geophys. Res. 80, 2478–2507.
Strom, R.G., Malin, M.C., Leake, M.A., 1990. Geologic map of the Michelangelo quadrangle of Mercury (H-15). Map I-2015, Misc. Investigations Ser., U.S. Geological Survey, Denver, Colo.
Strom, R.G., Chapman, C.R., Merline, W.J., Solomon, S.C., Head, J.W., 2008. Mercury cratering record viewed from MESSENGER's first flyby. Science 321, 79–81.
Trask, N.J., Dzurisin, D., 1984. Geologic map of the Discovery quadrangle of Mercury (H-11). Map I-1658, Misc. Investigations Ser., U.S. Geological Survey, Denver, Colo.
Trask, N.J., Guest, J.E., 1975. Preliminary geologic terrain map of Mercury. J. Geophys. Res. 80, 2461–2477.
Wagner, R., Head, J.W., Wolf, U., Neukum, G., 2002. Stratigraphic sequence and ages of volcanic units in the Gruithuisen region of the Moon. J. Geophys. Res. 107, 5104. doi:10.1029/2002JE001844.
Watters, T.R., Murchie, S.L., Robinson, M.S., Solomon, S.C., Denevi, B.W., André, S.L., Head, J.W., 2009. Emplacement and tectonic deformation of smooth plains in the Caloris basin, Mercury. Earth Planet. Sci. Lett. 285, 309–319 (this issue).
Whitford-Stark, J.L., Head, J.W., 1980. Stratigraphy of Oceanus Procellarum basalts: sources and styles of emplacement. J. Geophys. Res. 85, 6579–6609.
Widdowson, M., Walsh, J.N., Subbarao, K.V., 1997. The geochemistry of Indian bole horizons: palaeoenvironmental implications of Deccan intravolcanic palaeosurfaces. In: Widdowson, M. (Ed.), Palaeosurfaces: Recognition, Reconstruction and Palaeoenvironmental Interpretation. Special Publication, vol. 120. Geological Society of London, pp. 269–281.
Wilhelms, D.E., 1976. Mercurian volcanism questioned. Icarus 28, 551–558.
Wilhelms, D.E., McCauley, J., 1971. Geological map of the near side of the Moon. Map I-703, Misc. Investigations Ser., U.S. Geological Survey, Denver, Colo.
Wilson, L., Head, J.W., 1981. Ascent and eruption of basaltic magma on the Earth and Moon. J. Geophys. Res. 86, 2971–3001.
Wilson, L., Head, J.W., 2008. Volcanism on Mercury: a new model for the history of magma ascent and eruption. Geophys. Res. Lett. 35, L23205. doi:10.1029/2008GL035620.
Wilson, L., Scott, E.D., Head, J.W., 2001. Evidence for episodicity in the magma supply to the large Tharsis volcanoes. J. Geophys. Res. 106, 1423–1433.
Yingst, R.A., Head, J.W., 1997. Volumes of lunar lava ponds in South Pole–Aitken and Orientale basins: implications for eruption conditions, transport mechanisms and magma source regions. J. Geophys. Res. 102, 10,909–10,931.
Yingst, R.A., Head, J.W., 1998. Characteristics of lunar mare deposits in Smythii and Marginus basins: implications for magma transport mechanisms. J. Geophys. Res. 105, 11,135–11,158.
Yingst, R.A., Head, J.W., 1999. Geology of mare deposits in South Pole–Aitken basin as seen by Clementine UV/VIS data. J. Geophys. Res. 104, 18,957–18,979.
Young, J.W., Mattingly, T.K., Duke, C.M., 1972. Crew observations. Apollo 16 Preliminary Science Report, Special Publication SP-315. NASA, Washington, D.C., pp. 5-1–5-6.